Non-Destructive Testing of metallic structures based on electromagnetic computational
methods

Submitted for the Degree of
Doctor of Philosophy by Means of Published works
At the University of Northampton

2021

Xiaobai Meng

To my late grandfather, who devoted his entire life to science, technology, and engineering.

DECLARATION

I hereby declare that the work described in this thesis is original work undertaken by me for the degree of Doctor of Philosophy by Means of Published works, at the Faculty of Art, Science and Technology – University of Northampton, United Kingdom. No part of the material described in this thesis has been submitted for any award of any other degree or qualification in this or any other University or College of advanced education.

Xiaobai Meng

ACKNOWLEDGEMENTS

PUBLICATIONS

Co-first author   * Corresponding author

[1] M. Lu[1], **X. Meng**[1], W. Yin*, Z. Qu, F. Wu, J. Tang, H. Xu, R. Huang, Z. Chen, Q. Zhao, Z. Zhang, A. Peyton, Thickness measurement of non-magnetic steel plates using a novel planar triple-coil sensor, NDT & E International, vol. 107, pp. 102148, 2019. (Co-first author)

[2] W. Yin[1], **X. Meng**[1], M. Lu*, Q. Zhao, H. Xu, Z. Zhang, A. Peyton, Permeability invariance phenomenon and measurement of electrical conductivity for ferrite metallic plates, Insight, vol. 61, pp. 472-479, 2019. (Co-first author)

[3] M. Lu, W. Yin*, A. Peyton, Z. Qu, **X. Meng**, Y. Xie, P. Zhao, J. Luo, Q. Zhao, Y. Tao, T. Zhou, Z. Zhang, A model for the triboelectric nanogenerator with inductive load and its energy boost potential, Nano energy, vol. 54, pp. 103883, 2019. (Cover featured article)

[4] W. Yin, M. Lu*, L. Yin, Q. Zhao, **X. Meng**, Z. Zhang, A. Peyton, Acceleration of Eddy Current Computation for Scanning Probes, Insight, vol. 60, pp. 547 – 555, 2018.

[5] L. Yin, B Ye, S. Rodriguez, R. Leiva, **X. Meng**, R. Akid, W. Yin, M. Lu*, Detection of Corrosion Pits Based on an Analytically Optimised Eddy Current Sensor, Insight, vol. 60, pp. 561– 567, 2018.

[6] H. Xu, M. Lu, J. R. Avila, **X. Meng**, W. Yin, Imaging Weld Cross-Section Using a Novel Frequency Feature in Multi-Frequency Eddy Current Testing, Insight, vol. 61, pp.738–743, 2019.

[7] M. Lu,[1]*, **X. Meng**[1], L. Chen, R. Huang, W. Yin*, A. Peyton, Measurement of ferromagnetic slabs permeability based on a novel planar triple-coil sensor, IEEE Sensors Journal, vol. 20, pp. 2904– 2910, 2020. (Co-first author)

[8] Z. Jin, Y. Meng, R. Yu, R. Huang, M. Lu*, H. Xu, **X. Meng**, Q. Zhao, Z. Zhang, A. Peyton, W. Yin, Methods of Controlling Lift-Off in Conductivity Invariance Phenomenon for Eddy Current Testing, IEEE Access, vol. 8, pp. 122413-122421, 2020.

[9] M. Lu, L. Chen, **X. Meng**, R. Huang*, A. Peyton, W. Yin*, Thickness measurement of metallic film based on a high-frequency feature of triple-coil electromagnetic eddy current sensor, IEEE Transactions on Instrumentation and Measurement, vol. 70, 2021. DOI: 10.1109/TIM.2020.3027929

[10] M. Lu, **X. Meng**, R. Huang, L. Chen, A. Peyton, W. Yin*, Measuring lift-off distance and electromagnetic property of metal using dual-frequency linearity feature, IEEE Transactions on Instrumentation and Measurement, vol. 70, 2021. DOI: 10.1109/TIM.2020.3029348

[11] M. Lu*, **X. Meng**, R. Huang*, L. Chen, A. Peyton, W. Yin*, Lift-off tolerant pancake eddy-current sensor for the thickness and spacing measurement of nonmagnetic plates, IEEE Transactions on Instrumentation and Measurement, vol. 70, 2021. DOI: 10.1109/TIM.2020.3033377

[12] M. Lu*, **X. Meng**, R. Huang*, L. Chen, A. Peyton, W. Yin*, Inversion of distance and magnetic permeability based on material-independent and lift-off insensitive algorithms using eddy current sensor, IEEE Transactions on Instrumentation and Measurement, vol. 70, 2021. DOI: 10.1109/TIM.2020.3036099

[13] **X. Meng,** M. Lu, W. Yin, A. Bennecer*, K. J. Kirk*, Inversion of lift-off distance and thickness for non-magnetic metal using eddy current testing, IEEE Transactions on Instrumentation and Measurement, vol. 70, 2021. DOI: 10.1109/TIM.2020.3038289

[14] M. Lu*, **X. Meng**, R. Huang, J. R. Avila, Z. Chen, L. Chen, A.J. Peyton, W. Yin*, Determination of surface crack orientation based on thin-skin regime using triple-coil drive-pickup eddy-current sensor, IEEE Transactions on Instrumentation and Measurement, vol. 70, 2021. DOI:10.1109/TIM.2020.3044729

[15] M. Lu*[1], **X. Meng**[1], R. Huang, J. R. Avila, Z. Chen, L. Chen, A. Peyton, W. Yin*, Restoration of surface crack depth for non-magnetic metal from thin-skin imaging using eddy current T-R sensor, IEEE Transactions on Instrumentation and Measurement, in press, 2020.

[16] M. Lu[1], **X. Meng**[1], R. Huang, L. Chen, A. Peyton, W. Yin*, A high-frequency phase feature for the measurement of magnetic permeability using eddy current sensor, NDT & E International, in press, 2020.

[17] M. Lu*[1], **X. Meng**[1], R. Huang*, L. Chen, A. Peyton, W. Yin, Thickness measurement of circular metallic film using single-frequency eddy current sensor, NDT & E International, vol. 119, p. 102420, 2021.

[18] M. Lu[1], **X. Meng**[1], R. Huang, L. Chen, A. Peyton, W. Yin*, Lift-off invariant inductance of steels in multi-frequency eddy-current testing, NDT & E International, in press, 2020.

[19] L. Chen, **X. Meng**, M. Lu*, Q. Ran, X. Liu, W. Yin, Development of a Novel Angle-Sensing Capacitive Sensor with Flexible Electrodes, in press, 2020.

[20] **X. Meng***, M. Lu, W. Yin, A. Bennecer, K.J. Kirk, Evaluation of coating thickness using lift-off insensitivity of eddy current sensor, Sensors, vol 21, no. 2, p. 419, 2021.

ABSTRACT

This thesis explores research published between 2018 to 2021 and focuses on electromagnetic (EM) computational methods in the field of non-destructive testing (NDT).

Conductive samples affect the electromagnetic field generated by coils with alternating induced currents. Referring to eddy current effects, materials with different properties (magnetic permeability, electrical conductivity, thickness) result in different secondary electromagnetic fields (influenced by the eddy current) and induced voltages on coils. Based on this fact, various methods have been developed to interrogate conductive samples (particularly for steels) using electromagnetic eddy current sensors. Compared to other NDT techniques that evaluate samples, the EM eddy current technique is employed to test good conductors such as steel. This research places an emphasis on the efficient and accurate EM computational methods for the EM field simulation (or the computation of impedance or voltage on coils) and retrieval of conductivity, permeability, and thickness for both nonferromagnetic and ferromagnetic steels.

For the EM simulation, a robust acceleration method was developed to hasten the edge-element finite element method (FEM). The main objective of the EM simulation is the development of a novel forward solver that can efficiently simulate how the EM properties (magnetic permeability, electrical conductivity, thickness, and lift-off) affect the detected signal (voltage or impedance) under different frequencies. The solver exploited an optimised initial guess to accelerate the EM eddy current computation for probes scanning (over a metallic plate) process. The bi-conjugate gradients stabilised (BICGS) method was utilised in solving the equation of finite-element sparse matrices - matrices forms of the Galerkin's equations (i.e., the fundamental formulas of EM FEM). Conventional methods start iterations with an initial guess of the vector potential (and electric scalar potential) at the default value (a zero vector). Based on the fact that the eddy current (or electromagnetic field) solutions under the adjacent position steps of the probe (for the scanning process) are very similar, the solution from the previous position step of the probe was assigned to be an initial guess for the next position step of the probe. As a result, the iterations in each solving process start from an optimised guess and smaller residuals (hasten the convergence) and thus nearly 40 % of the computation time were reduced.

Simplified algorithms (embedded in the system) were introduced for the retrieval of conductivity, permeability, and thickness of steels. The simplified formulation has its merits of high computation speed, and solving the lift-off effect on the property retrieval in the production process of steels when using custom-designed EM sensors. Both the swept-frequency (or multi-frequency) and single-frequency impedance were used for the sensitivity analysis of spectrum and real-time retrieval of EM properties. Various features, retrieval strategies, and EM eddy current sensors were used for different conditions on the property retrieval. Firstly, a new permeability Invariance Phenomenon was discovered and investigated in the Dodd-Deeds method (analytical formulas of the impedance for circular coils horizontally deployed above the steel plate) when using a custom-built sensor (driving-pickup sensor, i.e., transmitter and receiver are horizontally spaced on the same height), which tackled the solution uniqueness problem due to the coupling impact of the sample's electrical conductivity and magnetic permeability. Based on this phenomenon, the electrical conductivity of ferromagnetic samples was measured without knowing its permeability. Secondly, several novel sensors were designed to reduce the lift-off effect on the property retrievals. By combining the measurement of different sensing pairs (considering sensitivities to lift-offs and test pieces), the thickness of the non-magnetic samples and the parameters of ferromagnetic slabs were retrieved using the simplified formulas. The error of the retrieved thickness (of non-ferromagnetic laminates) is 1.4 % for lift-offs up to 15 mm when using the triple-coil sensor, and 5.4 % for lift-offs up to 12 mm when using the single transmitter-receiver sensor.

Table of Contents

Abbreviation

NDT	Non-destructive Testing
NDE	Non-destructive Evaluation
EM	Electromagnetic
ECT	Eddy current testing
MFL	Magnetic flux leakage
RFT	Remote field testing
MPT	Magnetic particle inspection
ACFM	Alternating current field measurement
ACPD	Alternating current potential difference
RFEC	Remote field eddy current
PECT	Pulsed eddy current testing
MECT	Multi-frequency eddy current testing
RCF	Rolling contact fatigue
ROT	Runout table
SQUIDS	Superconducting quantum interference devices
TMR	Tunnel magneto resistive
SNR	Signal-to-noise ratio
LOI	Lift-off point of intersection
PF	Peak frequency
ZCF	Zero-crossing frequency
FE	Finite element
BE	Boundary element
MCS	Multi-layered conductive structures
SOTC	Second-order transmission condition
DDM	Domain decomposition method
NC	Non-conformal
TREE	Truncated region eigenfunction expansion
CIP	Conductivity invariance phenomenon
SII	Sample-independent inductance
MAS	Method of auxiliary sources
ILU	Incomplete lower-upper
BICGS	Bi-conjugate gradients stablished
MAXIT	Maximum interference threshold

List of Figures

List of Tables

Chapter 1 Review of Electromagnetic Non-Destructive Testing

1.1 Non-destructive testing

Nondestructive testing (NDT) or Nondestructive evaluation (NDE) is a wide group of analysis techniques used in science, and technology industry to evaluate a material, component or system without causing damage, cutting apart, or otherwise altering the material (Cartz,1995,pp.1-5). NDT methods are routinely applied in industries where a failure of a component would cause significant hazard or economic loss, such as in transportation, pressure vessels, building structures, piping, and hoisting equipment.

NDT has been successfully implemented in diverse industrial activities (Blitz and Simpson,1995,pp.1-4), including the inspection and measurement of raw materials or components during production (e.g. the stress cracking, porosity defect, cinder inclusion, weld junction) (Hull and John, 2015,pp.1-6), testing of the mechanical and civil structures (e.g. turbo machinery), and visualization in medical procedures (e.g. radiography, and ultrasonic testing). In addition, NDT can reveal defects of machining error, heat treatment, incorrect assembly parts, defects of paintings in art (Sfarra et al.,2014), and can produce images of cross section welds (Hull and John, 2015,pp.1-6).

Various techniques including the electromagnetic, ultrasonic and acoustic (or mechanical), optical, and chemical methods have been frequently used in the field of NDT. For the identification and measurement of cracks, surface cavities, internal voids defective welds, and any type of flaw which would lead to premature failure, commonly used NDT techniques are listed in Table 1 (Dwivedi, Vishwakarma, and Soni,2018).

Table 1 Commonly used NDT techniques

NDT Techniques	Capabilities	Limitations
Ultrasonic testing	Subsurface flaws	Material must be good conductor of sound.
Electromagnetic testing	Surface and near surface flaws	Difficult to interpret the detected signal in some applications; only for metals.
Acoustic testing	Can analyse entire structure	Difficult to interpret the detected signal; expensive equipment.
Radiography	Subsurface flaws	Depth of defect should be over 2 % of the thickness; it needs radiation protection; it is not suitable for subsurface flaws and porous materials.
Optical Inspection	Macroscopic surface flaws	Small flaws are difficult to detect; it is not suitable for subsurface flaws.

As an important tool in the NDT repository, the electromagnetic testing technique interrogates the sample with electric and magnetic fields to observe the electromagnetic (EM) properties of the material, particularly conductive and magnetic permeable materials. Owing to its sensitivity to small discontinuities, EM NDT has been widely applied in object recognition, health monitoring, surface fatigue inspection, and measuring inhomogeneity of metallic properties including electrical conductivity, magnetic permeability, and thickness of the sample.

1.2 Comparison of Electromagnetic NDT techniques

There exist several variants of the EM NDT method (Liu et al.,2017), including eddy current testing (ECT), magnetic flux leakage (MFL), remote field testing (RFT), magnetic particle inspection (MPT), alternating current field measurement (ACFM), alternating current potential difference (ACPD) (Bowler,2006), and Direct Current Potential Drop (DCPD) (Vassilaros et al.,1984).

1.2.1 Magnetic flux leakage

As shown in Fig. 1, magnetic flux leakage (MFL) is a magnetic method of EM NDT that is used to detect corrosion and pitting in steel structures, most commonly pipelines and storage tanks (Liu et al.,2017). The basic working principle is that a powerful magnet is used to magnetize the metal. In areas where there is a discontinuity of surface (e.g., corrosion or missing metal), subsurface or far surface (e.g., in storage tank floors), the magnetic field is perturbed, which can be detected by the hall probe (Fig. 1) (Sekine, Kasai, and Maruyama,2000). The magnetic leakage field can be detected by MFL sensors placed between the poles of

the magnet (Udpa and Stanley,2004). Commonly used MFL sensors include Hall probes and Magnetic Particle Inspection (MPI). MFL is suitable for quantifying the size of surface defect for ferromagnetic materials. However, the properties of sample (e.g., electrical conductivity or magnetic permeability) need to be retrieved in prior (which is measured using eddy current sensors in this thesis) for quantifying the defect size, as both properties and defect size affect the sensor signal.
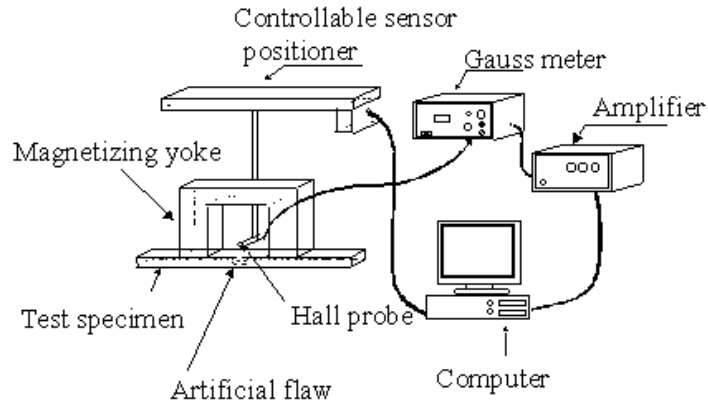
Figure 1 Schematic plot of magnetic flux leakage technique (Sekine, Kasai, and Maruyama,2000)

1.2.2 Remote field testing

Remote field testing (RFT), also termed as remote field eddy-current (RFEC) testing, is an EM NDT technique using low-frequency alternating current excitations. Owing to the low working frequency, the magnetic field generated by the transmitter coil (or excitation coil) can penetrate the thick pipe wall and transmits along the outside of the pipe (as shown in Fig. 2). A receiver coil is used to detect the magnetic field travelled back from the outside of the pipe wall (thus a total of two penetrating-wall transmissions). Moreover, eddy currents induced from the excitation coil generates a secondary reverse magnetic field that tends to attenuate the primary magnetic field transmitted inside the pipe (as shown in the direct energy transmission path of Fig. 2). At a travel distance of two to three pipe diameters, the direct magnetic field nearly vanished. Thus, the magnetic field sensed by the detector is mainly contributed by the indirect transmission field from outside of pipes.
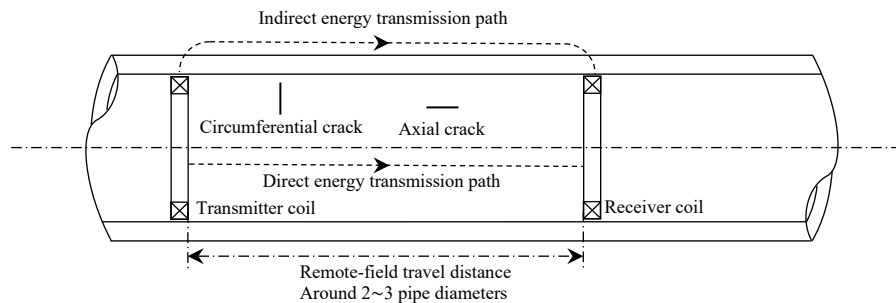
Figure 2 Schematic plot of remote field eddy-current testing (Xu et al.,2014)

As a non-contact sensing technique, RFT is able to detect inside and outside defects (but cannot distinguish them) with approximately equal sensitivity. Moreover, RFT is less sensitive to the effect of probe wobble for the coil inside pipes. However, since the magnetic field transmits outside of the pipe, RFT shows reduced accuracy because of sensitivity to conductive and magnetic objects on or near the outside of the pipe, such as attachments or tube support plates. Because the induced eddy current is axially concentric with the pipe, RFT is more sensitive to the axial crack than to the circumferential crack. RFT is commonly used for detecting or determining the size of defects on small-diameter steel tubes and pipeline pigging (Kim, Udpa, and Udpa,2004). However, the properties of tube or pipe, including the electrical conductivity, magnetic permeability (for ferromagnetic materials), dimensions (diameter and thickness) are needed for the defect quantification (as defect size and material properties affect the measured coil signal), which is retrieved using eddy current testing in this thesis.

1.2.3 Alternating current field measurement

Alternating current field measurement (ACFM) is an EM technique for NDT detection and size (and depth) measurement of the surface breaking cracks. ACFM was derived from ECT and applies to both non-ferromagnetic (e.g., austenitic materials with unit relative permeability) and ferromagnetic metals. As shown in Fig. 3, the ACFM probe induces a uniform alternating eddy current in the region under test and detects the magnetic field near the surface. The induced eddy current is undisturbed if the region is defect free. The presence of a surface crack will redirect the induced eddy current around the edge and middle of the crack. The ACFM probe measures disturbances in the magnetic field (both lateral B_x and vertical B_z) and uses mathematical modelling to estimate crack depth and size (Papaelias et al.,2009).
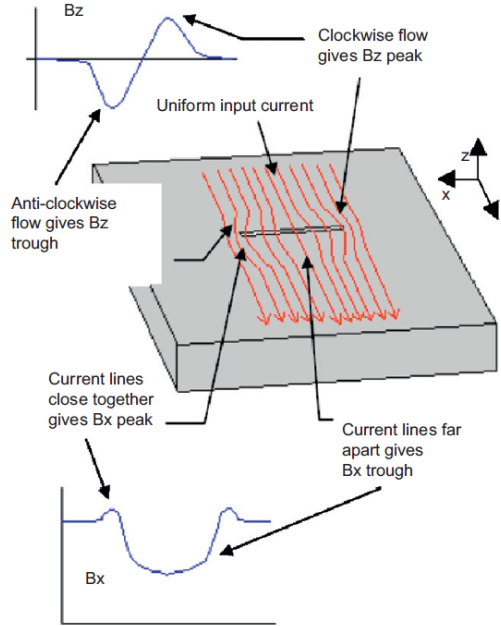
Figure 3 Schematic plot of alternating current field measurement (Papaelias et al.,2009)

As a non-contact sensing technique, ACFM is non-invasive and can be applied to inspect (paint) coated and hot-surface metals. Moreover, ACFM can estimate the depth and length of surface defects of any metals. The measured data can be used for the offline evaluation (if necessary) and permanent record indications. However, the size of the ACFM probe makes it difficult to inspect the defect within short (or narrow) or small samples. Besides, multiple close defects (clusters) reduce the ability to estimate the defect depth. Moreover, ACFM is affected by the lift-off (the spacing distance between the conductor and sensor). Overall, ACFM is used for characterising surface defects of good conductors, while the properties of conductors (thickness, electrical conductivity, and magnetic permeability) are required for retrieving the size of defect (which is measured using eddy current sensors in this thesis).

1.2.4 Alternating current potential difference

Alternating current potential difference (ACPD) is an EM NDT technique making use of skin depth to determine the size (particularly the depth) of a crack. In this technique, an alternating current with constant amplitude is injected into the metal through two current electrodes (also termed as the electrical contact) placed on either side of the crack (equidistant and perpendicular to the crack orientation), as shown in Fig. 4 a). A voltage meter is used to measure the potential difference between voltage electrodes (close and perpendicular to the crack; and separated by a constant distance of s) is measured for both crack and crack-free regions. The crack depth, d is obtained by using the following equation (Raja et al.,2010).

$$d = \frac{s}{2}\left(\frac{V_c}{V_o} - 1\right) \qquad (1.a)$$

where s is the separating distance of two voltage electrodes. V_c and V_o are the measured voltage for the crack and crack-free regions.

14

Because of the electrical contact, ACPD (Bowler, 2006) can apply relatively low frequency (a better SNR compared to ECT under low frequency; ECT needs a higher excitation current flowing in the coil for large lift-offs and under low frequencies, which could result in a risk of heating for the coil). However, the orientation of the crack must be identified accurately (which is measured by eddy current techniques presented in Chapter 5.2 of this thesis). Moreover, the surface of the test piece must very clean. Compared to ACFM technique, ACPD needs good electrical contact and calibration (because of the relative measurement). Thus, ACPD cannot work through coatings such as paint or rust.
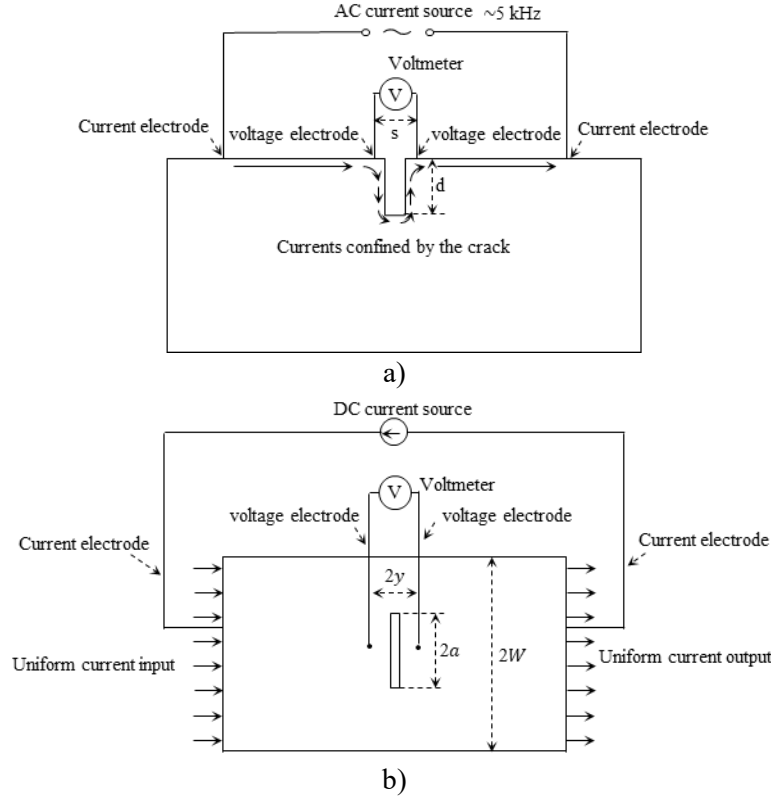
Figure 4 a) Schematic plot of alternating current potential difference (ACPD) technique b) Schematic plot of direct current potential difference (DCPD) technique

1.2.5 Direct Current Potential Drop

Direct Current Potential Drop (DCPD) is an EM NDT method for measuring crack extension (or growth). As shown in Fig. 4 b), direct-current (DC) electrodes are connected to the edge of specimen to generate uniform current input and output. Two voltage electrodes (aligning to the normal line of crack centre) are used to measure the potential drop (voltage). To convert the measurement of potential drop to the real-time crack growth size, the Johnson's calibration equation has been widely used (Johnson, 1965).

$$\frac{a}{W} = \frac{2}{\pi} cos^{-1} \left[\frac{cosh\left(\frac{\pi y}{2W}\right)}{cosh\left(\frac{V}{V_0} cosh^{-1}\left\{\frac{cosh\left(\frac{\pi y}{2W}\right)}{cosh\left(\frac{\pi a_0}{2W}\right)}\right\}\right)} \right] \tag{1.b}$$

where V, $2a$ is the instantaneous voltage (voltmeter) and length of crack, respectively. V_0, $2a_0$ is the initial voltage (voltmeter) and length of crack, respectively. $2W$ is the width of specimen. $2y$ is the separating distance of two voltage electrodes.

Compared to the ACPD method, DCPD is less sensitive to variants of magnetic permeability of specimen. This is because in the ACPD method, the induced current flow is confined to the surface of specimen due

to the eddy current skin effect. A technical term – skin depth is used to index the depth of the induced eddy current (discussed in equation 4 in the following section). A larger magnetic permeability of specimen results in a thinner skin depth.

As the five representative EM NDT methods, ECT, MFL, RFT, ACPD and DCPD have their Capabilities and limitations, as shown in Table 2 (Blitz, 2012,p.5,pp.132-156,pp.214-227; Liu et al.,2017).

1.2.6 Eddy current testing

Eddy current testing (ECT) (Blitz, 2012,p.5) is one of the most commonly used EM techniques, which has been used for the detection of near-surface cracks and corrosion in metallic objects such as tubes and aircraft fuselages and structures (Liu et al.,2017). Moreover, ECT has been widely used for the property measurement of both non-magnetic and ferromagnetic materials, including the thickness, electrical conductivity, and magnetic permeability (of magnetic materials).

Commonly used ECT techniques include pulsed eddy current testing (PECT) (Bowler and Johnson,1997; Knight, Brennan and Dover, 2004), and multi-frequency eddy current testing (MECT). As sketched in Fig. 5 (Pohl et al.,2004), when a circular conductive coil winding excited with an alternating current approaches an electrically conductive non-ferromagnetic material, the primary alternating magnetic field generated from the coil penetrates the material and induces alternating and circular currents (the similar geometry as the excitation coil). The induced current flowing near the surface of test piece, termed as the eddy current, generates a secondary magnetic field that tends to oppose the primary magnetic field. According to Lenz's law, the induced electromotive force, ϵ on the coil is weakened due to the secondary magnetic field generated from the eddy current. Variations in the electrical conductivity and magnetic permeability of the test object, and the presence of defects causes a change in eddy current and a corresponding change in phase and amplitude of ϵ that can be detected by measuring the impedance changes in the coil (Placko and Dufour,1992).

$$\epsilon = -N\frac{d\phi}{dt} \tag{2}$$

where N is the number of turns for the coil winding. ϕ denotes the magnetic flux generated from a single coil. $\frac{d\phi}{dt}$ is the change rate of the magnetic flux generated from a single coil.
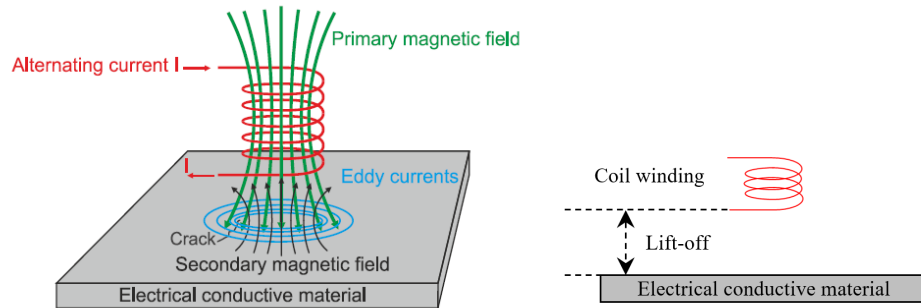
Figure 5 Primary and secondary magnetic field, with induced eddy currents near the surface of the test piece

As a non-contact sensing technique, ECT is suitable for the testing and evaluation of all metal materials. However, due to the skin effect of induced eddy currents (with the skin depth calculated by equation 4), ECT is commonly suitable for surface or near-surface defect detection. For the far-surface defect detection (e.g., external defect of heat exchanger tube), the frequency of excitation current should be controlled to ensure that the induced eddy current is deep enough to interact with the far-surface defect.

The density of induced eddy current, J attenuates exponentially with depth (Chew,1995,pp.4-10).

$$J = J_s e^{-(1+j)d/\delta} \tag{3}$$

where J_s is the density of the induced eddy current at the surface. d is the depth of the eddy current to be calculated. j is the imaginary unit. δ is the skin depth, which is defined as the depth below the surface of the conductor at which the current density (either the real part or the imaginary part) has fallen to 1/e (about

0.37) of J_s. The skin depth, δ is affected by both the EM properties of conductors and working frequency of the alternating current flowing in the excitation coil. Generally, the skin depth, δ is calculated via the following formula.

$$\delta = \frac{1}{\sqrt{\pi f \sigma \mu}}$$ (4)

where f is the working frequency of alternating current flowing in the excitation coil. σ and μ are the electrical conductivity and (absolute) magnetic permeability of the test piece.

Because of the non-contact sensing, the signal of ECT is sensitive to the lift-off (the spacing distance between the conductor and coil, as shown in Fig. 5). Further discussions of the lift-off effect are presented in section 1.3.4.

Table 2 Comparisons of ECT, MFL, RFT, ACFM, and ACPD techniques

NDT Techniques	Principles	Capabilities	Limitations
ECT	Induced eddy current effect	Non-contact sensing, suitable for automatic detection of all metal materials, easy assembling, portable, diverse applications including both the surface crack inspection and evaluation of metal properties.	Commonly suitable for surface or near-surface defect detection (due to skin effect), cannot use conductive shielding, sensitive to sensor lift-off
MFL	Leakage of magnetic field	Non-contact sensing, powerful penetration, can measure both internal and external defects of pipes, anti-interference for nonferromagnetic objects, can achieve automatic and high-speed inspection with non-ferromagnetic shielding such as copper and aluminium	Limited to ferromagnetic materials, additional magnetising devices are needed, and the magnetic attractive force is unavoidable
RFT	Transmission of low-frequency magnetic field	Non-contact sensing, powerful penetration, can measure both internal and external defects of pipes, less sensitive to the effect of probe wobble	Cannot distinguish internal and external defects, reduced accuracy and sensitivity at conductive and magnetic objects on or near the outside of the pipe, less sensitive to the circumferential crack of pipe
ACFM	Lateral and vertical magnetic field of perturbed eddy currents	Non-contact sensing, can apply to (paint) coated and hot-surface metals, non-invasive, can estimate the depth, size of surface defects of any metals, do not need calibration	Difficult to inspect the defect within short (or narrow) or small samples, difficult to estimate the depth of multiple close defects (clusters), welds and grindings can result in spurious indications
ACPD	Skin effect of injected AC current	Apply to a relatively low frequency without sacrificing SNR (because of electrical contact), avoid the risk of probe heating as only need a lower measuring current, avoid the lift-off effect	The orientation and location of the crack must be identified accurately, the surface of the test piece must very clean, need a good electrical contact (cannot work through coatings such as paint or rust), need calibration (relative measurement).
DCPD	With the injected DC current, measured potential drop is sensitive to the crack growth	Less sensitive to the magnetic permeability variants of specimen, avoid the risk of probe heating as only need a lower measuring current, avoid the lift-off effect	The orientation and location of the crack must be identified accurately, the surface of the test piece must very clean, need a good electrical contact (cannot work through coatings such as paint or rust), need calibration (relative measurement).

1.3 Review of eddy current testing

As one of the most used EM NDT techniques for the evaluation of metals, ECT plays an important role in numerous industries, particularly in rail, aerospace, petrochemical, nuclear, and transportation. Applications of ECT include the detection of surface or near-surface defects, measurement of thickness, electrical conductivity, and magnetic permeability of austenitic and ferromagnetic metals. As mentioned in section 1.2.5, the working principle of ECT is based on the variation of secondary magnetic field generated by the

induced eddy current (from the excitation coil) within the test piece. Variations in the electrical conductivity and magnetic permeability of the test object, and the presence of defects result in a change (both amplitude and phase) of the induced eddy current and secondary magnetic field, which can be detected by measuring the impedance change in the coil.

1.3.1 Industrial needs

Steel is one of the most important engineering materials. Being able to monitor the surface (or near-surface) defects and mechanical properties in real-time and in situ in steel production means the possibility to engineer desired steels through feedback and control.

1.3.1.1 Defect detection

The defect detection and measurement of its depth (size) and angle are vital in diverse non-destructive applications. For example, in the rail industry, cracks, particularly the rolling contact fatigue (RCF) have become prevalent due to increased traffic density and higher axle loads, which has resulted in derailment accidents (Nicholson and Davis,2012).

The characteristics of RCF cracks in rail (as shown in Fig. 6) place strong demands on inspection systems. RCF commonly occurs in closely spaced clusters. The spacing of cracks has a significant impact on distinguishing and retrieving the depth (or size) and angle of individual defects within the cluster. Depending on rail type and traffic conditions, spacings of individual RCF ranges from 0.8 mm to 20 mm. What's more, RCF defects may occur with slight variations of the rail running band and orientations. Moreover, RCF grows at random directions (angles to the longitudinal direction of the rail range from 30 to 75 degrees; angles to the circumferential direction of the wheel range from 30 to 90 degrees) (Nicholson and Davis,2012). Based on the ECT, the presence of surface crack affects the induced eddy currents and detected impedance from the coil. Thus, in principle, ECT can determine the depth (or size) of the surface (or near-surface) crack (Thomas, Dey, and Heyder,2010). In practice, it is vital to distinguish the effect of size and depth on quantifying RCF in rails. To grind the rail, the most important aspect for maintenance engineers is to find the normal depth. Given that RCF have different angles, the defect depth is commonly overestimated. Previously, the concentric eddy current sensor is suitable for quantifying the depth (from the peak value of measured voltage, where the defect is underneath the coil centre), but cannot retrieve the surface orientation of the crack (angle relatively to the scanning direction). In my published works (Chapter 5.2), a triple-coil driving-pickup eddy current sensor was designed to determine the surface orientation of the crack, which is based on the eddy current thin-skin regime. The relative error of the retrieved angle is 3.5 % (Lu et al.,2021).
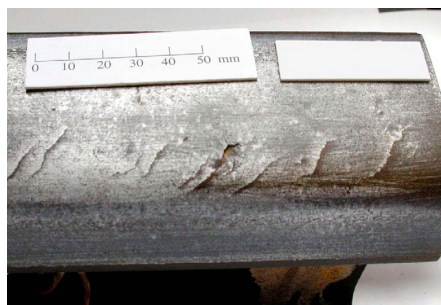
Figure 6 Typical RCF cracking in rails. (Papaelias et al.,2009)

1.3.1.2 Evaluation of metallurgical property
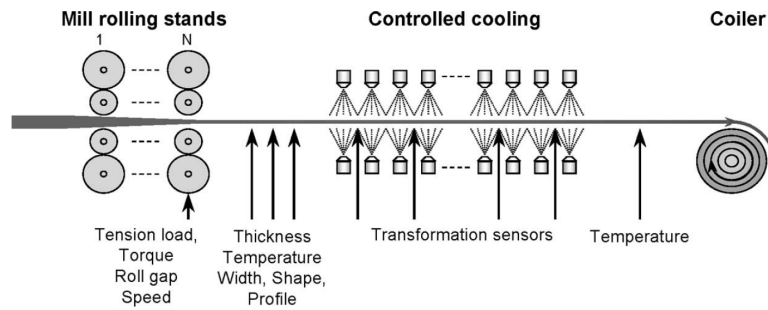
Figure 7 Schematic plot of a hot strip mill (Dickinson et al.,2007)

The hot strip mill is usually composed of three parts: reheat furnaces, mill rolling stands, and cooling zone, as shown in Fig. 7. In the furnaces, the cast slab is reheated to hot rolling temperature (nearly 1200 degrees). The mill rolling starts from the slab into the dimension required by customers with a fine-grained steel strip product. Then the strip is water cooled on the runout table (ROT) to ensure that it transforms into the desired grain structure (Dickinson et al.,2007). The mechanical properties such as strength and toughness of the final steel products are strongly dependent on their grain structures; thus, the cooling process should be accurately controlled. Therefore, to increase grain-structure homogeneity of steels, and thus improve consistency in the mechanical properties, significant advances in materials characterisation would be obtained if grain-structure information could be determined during steel production in a non-destructive and remote manner.

Besides, the characterisation of the steel grain structure is an important tool for metallurgists as mechanical properties are controlled by grain-structure parameters such as grain size, phase balance, and precipitates. ECT techniques provide the opportunity for monitoring phase transformation, by detecting changes in electrical conductivity and magnetic permeability within the steel. This is particularly useful because conductivity and permeability are known to be directly influenced by the steel grain structure. In the grain structure, the austenite grain is paramagnetic, whereas ferrite/pearlite, martensite, and bainite grains are ferromagnetic below the Curie temperature (Davis et al.,2002). Hence, an eddy-current sensor, based on magnetic induction and sensing coils, is able to detect the ferromagnetic phase change. Since the measured signal (impedance or inductance) of the eddy current sensor is significantly sensitive to the lift-off variation, novel measurement strategies or retrieval techniques are required to reduce the error (on the property retrieval) caused by lift-offs. E.g., in my published works (Chapter 4.2), by using a sample-independent inductance feature, the error on the thickness retrieval of non-magnetic plates is 5.4 % for lift-offs up to 12 mm when using a single transmitter-receiver sensor (Meng et al.,2021).

1.3.2 ECT probes

Various configurations are presented for the excitation source and detection sensor of ECT probes. In most applications, inductive coils are utilized both as a field source and field sensors. An inductive probe can include one or more coils. In conventional ECT probes, these coils typically comprise lengths of wire wound in a helical manner like a solenoid. The winding will commonly have more than one layer to increase the value of inductance. ECT probes are commonly classified according to their configuration and mode of operation. The probe configuration is closely related to the testing area of interest using coils.

1.3.2.1 Encircling coil probes for bars, tubes, or pipes

For the inspection of tubes, bars, pipes, and cylindrical conductors (including co-axially multilayer cylinders), the standard ECT probe is the encircling coil winding. Different encircling probes are designed for researchers and manufacturers to monitor discontinuities in products with various profiles and geometries (Fig. 8). Since the induced eddy current is circumferential (and opposite to the excitation current), encircling coils are sensitive to axial discontinuities (parallel to the axis of the tube or bar). External encircling-coil ECT probes are typically used for the inspection of the thin bar or wire. Considering the potential interference of the conductive and magnetic objects on or near the outside of the pipe, encircling-coil ECT probes are commonly used.
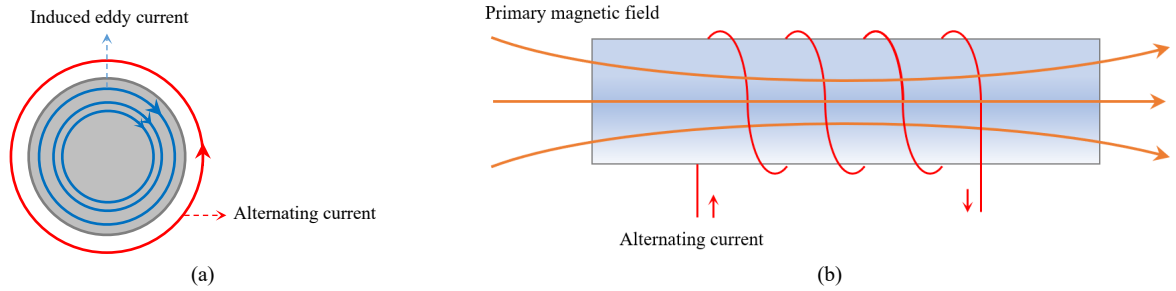
Figure 8 (a) Induced eddy current of external encircling coil (b) Schematic plot of an external encircling coil for the inspection of bar or pipe

Internal encircling-coil probes mostly apply to the inspection of defects on or near the inner surface of the tube. The commonly used internal encircling-coil probes include bobbin probes (both differential and absolute bobbin probes), array probes, mechanical rotating probes, and rotating field probes.

As shown in Fig. 9 (a), the differential bobbin probe has two identical coils with alternative currents of the same magnitude but out of phase. The probe is sensitive to small defects and less affected by the probe wobble (as shown in Fig. 9 c). However, the probe is less sensitive to the changes of material properties. In Fig. 9 (b), the absolute bobbin probe is sensitive to both defects and material properties (including the electrical conductivity, magnetic permeability, and thickness of pipe wall). However, the absolute bobbin probe is sensitive to the wobble effect of probes. The capabilities and limitations of commonly used internal encircling-coil probes are listed in Table 3.
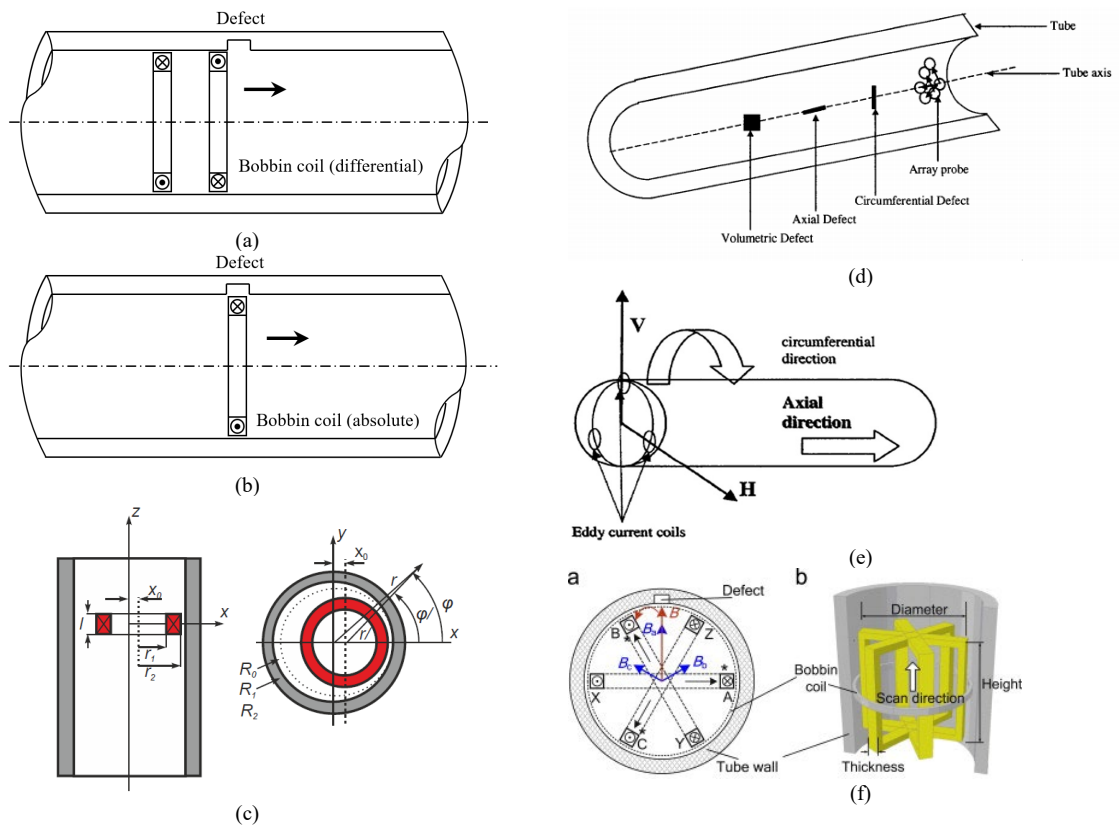
Figure 9 Schematic plot of (a) Differential bobbin-coil probe (b) Absolute bobbin-coil probe (c) Wobble effect: a bobbin coil in an offset position to a tube (García-Martín, Gómez-Gil, and Vázquez-Sánchez,2011) (d) Array probe (Jella,2004,p.32) (e) Mechanical rotating probe (AbdAlla et al.,2019) (f) Rotating field probe (Xin et al.,2013)

Table 3 Comparisons of internal encircling-coil probes for the assessment of tube or pipe

Probe types	Capabilities	Limitations
Bobbin probe	Rapid inspection, can retrieve defect depth and length, economical, sensitive to axial flaws	One-dimension scan data, insensitive to circumferential defect
Array probe	Sensitivity to defects of all orientations, rapid inspection, can	Costly, complicated instrument

	retrieve defect depth and size from the internal surface of pipe using the C-scan imaging	
Mechanical rotating probe	High image resolution, sensitivity to defects of all orientations, higher SNR	Limited inspection speed, costly
Rotating field probe	Rapid inspection, sensitivity to defects of all orientations, do not need to mechanically rotate the probe, high inspection speed	Difficult to measure the depth of the defect on the external surface of the pipe

1.3.2.2 Pancake coil probes for slabs
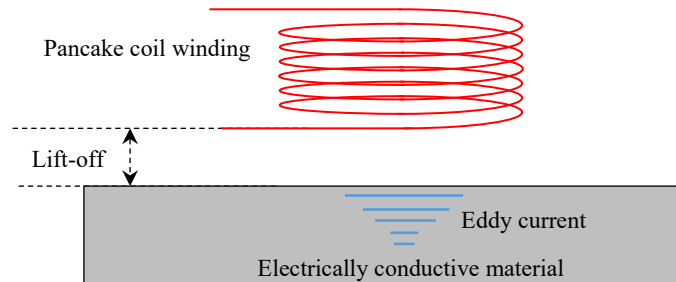
Figure 10 Schematic plot of the pancake coil above the electrically conductive material

For the assessment of metallic slabs, pancake-coil probes (Fig. 10) are commonly used. The probe is placed above the metal slab with the coil axis perpendicular to the surface of the test piece. Pancake probes can be either air-core coils or ferrite-core coils. As ferrites have high magnetic permeability, the initial coil impedance of ferrite-core coil is higher than of air-core coils. Pancake-coil probes are very sensitive to the lift-off and inclination with respect to the flat surface.

1.3.2.3 Other ECT probes

For different applications, other types of probes are used, including solenoid exciting coil for probes, superconducting quantum interference devices (SQUIDs) for the sensing coil of probes, Hall-effect and magneto resistive sensors (García-Martín, Gómez-Gil, and Vázquez-Sánchez,2011) for the sensing coil of probes. For example, magneto resistive sensors, particular the tunnel magneto resistive (TMR) sensors have been used for the receiver of the ECT probe, which have a higher SNR for the measurement of weak magnetic field under low excitation frequencies (compared to the coil type sensors).

(a)

(b)
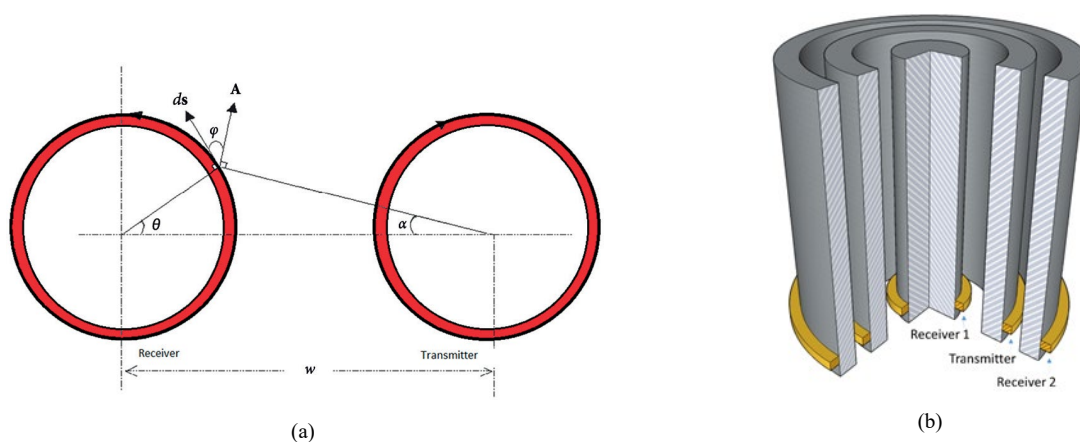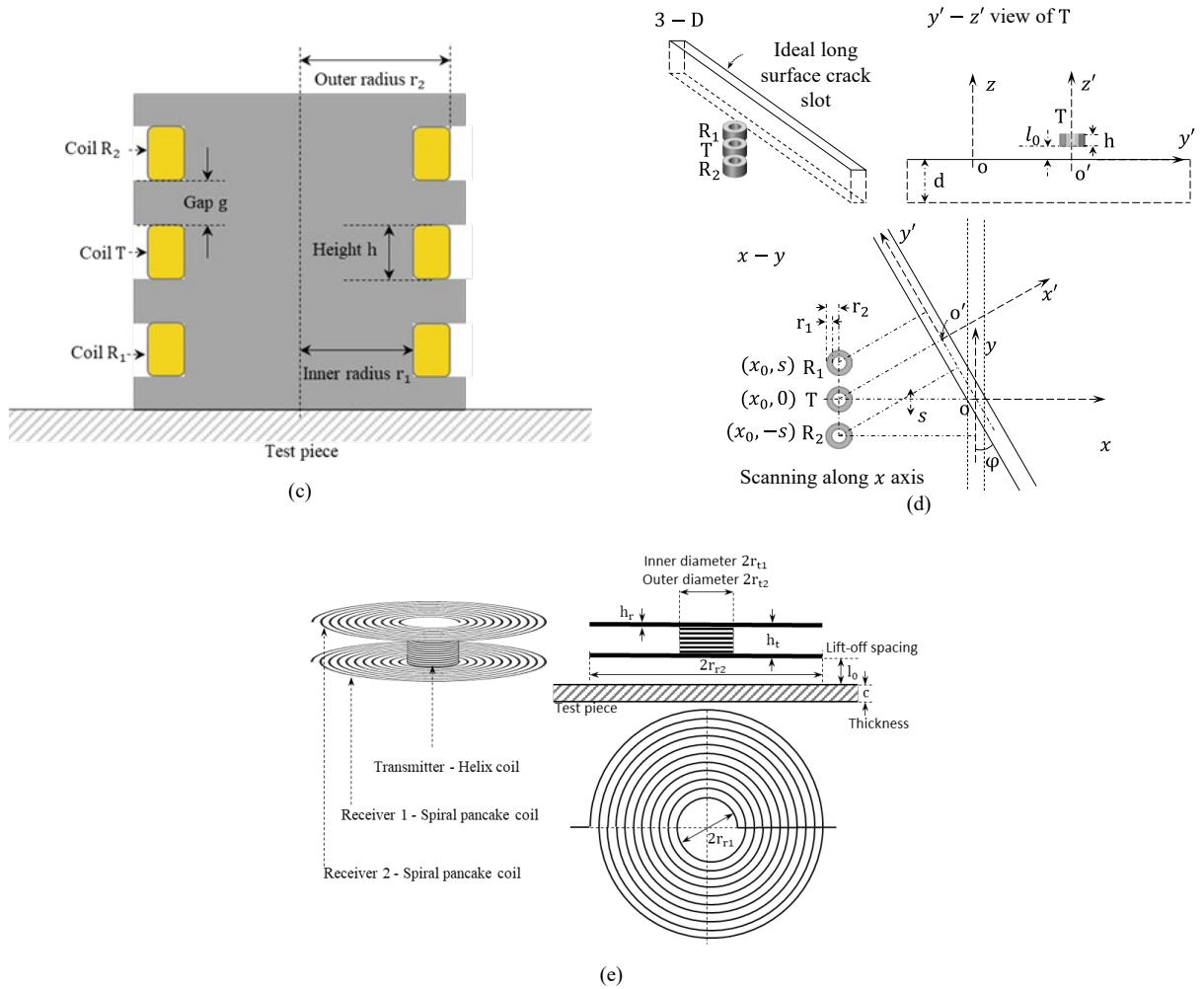
Figure 11 (a) Drive-pickup eddy current probe (Yin, Meng et al.,2019) (b) planar triple-coil eddy-current sensor (Lu, Meng et al.,2020) (c) triple-coil concentric (or helix) probe (Lu et al.,2021) (d) triple-coil drive-pickup probe (Lu et al.,2021) (e) triple-coil pancake probe (Lu et al.,2021)

In my published works (Chapter 3, 4, 5), features and formulas for the property retrieval and surface-defect inspection of steels are based on different custom-built eddy current probes, including drive-pickup probe (Fig. 11 a) for retrieving the electrical conductivity (while the permeability is unknown), planar triple-coil eddy-current sensor (Fig. 11 b) and triple-coil concentric (or helix) probe (Fig. 11 c) for the property retrieval while reducing lift-off effects, triple-coil drive-pickup probe (Fig. 11 d) for the determination of surface-crack orientation, and the triple-coil pancake probe (Fig. 11 e) for the signal augmentation (for lift-offs over 10 mm). E.g., in Fig. 11 (Yin, Meng et al.,2019), the permeability invariant phenomenon (PIP) is found for the first time when using the driving-pickup eddy current probes.

1.3.3 ECT techniques

1.3.3.1 Pulsed eddy current

The conventional eddy-current equipment uses sinusoidal alternating excitation which is limited by the skin effect of eddy currents. Consequently, the conventional ECT is commonly used for the detection of surface or near-surface defect of millimetres deep. As mentioned in equation (4), the skin depth increases with lower frequencies. However, referring to Lenz's law in equation (2), a lower excitation frequency leads to a reduced induced voltage, which results in a reduced SNR (García-Martín, Gómez-Gil, and Vázquez-Sánchez,2011).

Compared to the conventional eddy-current instrument, pulsed instruments generate a square, triangular, or sawtooth waveform, which has a broad spectrum of frequencies. Thus, pulsed eddy current (PEC) testing

provides more information than the conventional ECT (García-Martín, Gómez-Gil, and Vázquez-Sánchez,2011).

The Pulsed Eddy Current (PEC) technique is an effective method of quantifying defects in multi-layer structures. The pulsed eddy current signals have common features in the transient characteristics such as the peak amplitude, time-to-peak amplitude, and time-to-zero crossing. The peak amplitude determines the defect size. The defect depth or material thickness can be retrieved from the peak amplitude (Bowler and Johnson,1997). The earliest study of PEC for crack detection in layered structures with installed fasteners was conducted by Harrison (Harrison,1994). Giguere et al. also studied the detection of cracks beneath rivet heads using the transient EC techniques (Giguere et al.,2002). Fig. 12 (a) and (b) show examples of different pulse width excitations and Amp with different pulse width. However, like most of the ECT sensors, PEC sensor is sensitive to the lift-off distance to the surface of the test piece.

(a)   (b)
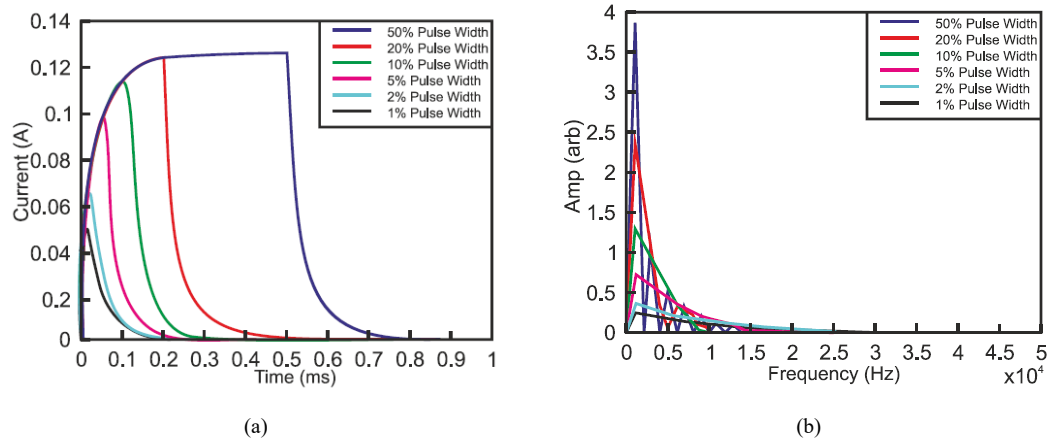
Figure 12 (a) Excitation currents input with different pulse width (b) Amp with different pulse width (García-Martín, Gómez-Gil, and Vázquez-Sánchez,2011).

1.3.3.2 Multi-frequency eddy current

Multi-frequency eddy current (MEC) testing operates at two or more test frequencies, which expands the capabilities of single-frequency testing (for the purpose of using different skin depths). MEC can apply to the real-time measurement as they allow simultaneous tests using multi channels. Besides, MEC can eliminate the undesired effect (caused by the probe lift-off, variations in temperature and geometries of the test piece) by analysing the probe response (for the analysis of varying parameter sensitivities under different frequencies) under an extensive range of frequencies (commonly from 100 Hz to 5 MHz) (Liu et al.,1999; García-Martín, Gómez-Gil, and Vázquez-Sánchez,2011). Thus, compared to PEC, MEC has a relatively high SNR particularly under high working frequencies (Rodriguez et al.,2014).

In my published works (Chapter 3.4), material-independent and lift-off insensitive algorithms were used to retrieve the lift-off and magnetic permeability of steels, which were based on multi-frequency inductance of the triple-coil (concentric) eddy current probe. The relative error on the permeability retrieval is 0.6 % for lift-offs up to 12 mm. (Lu et al.,2021) The lift-off insensitive inductance feature (where inductance change curves of one sample at different lift-offs intersects at one point; the intersected points for all samples share the same inductance value, which is dependent on the sensor parameter) is shown in Fig. 13.
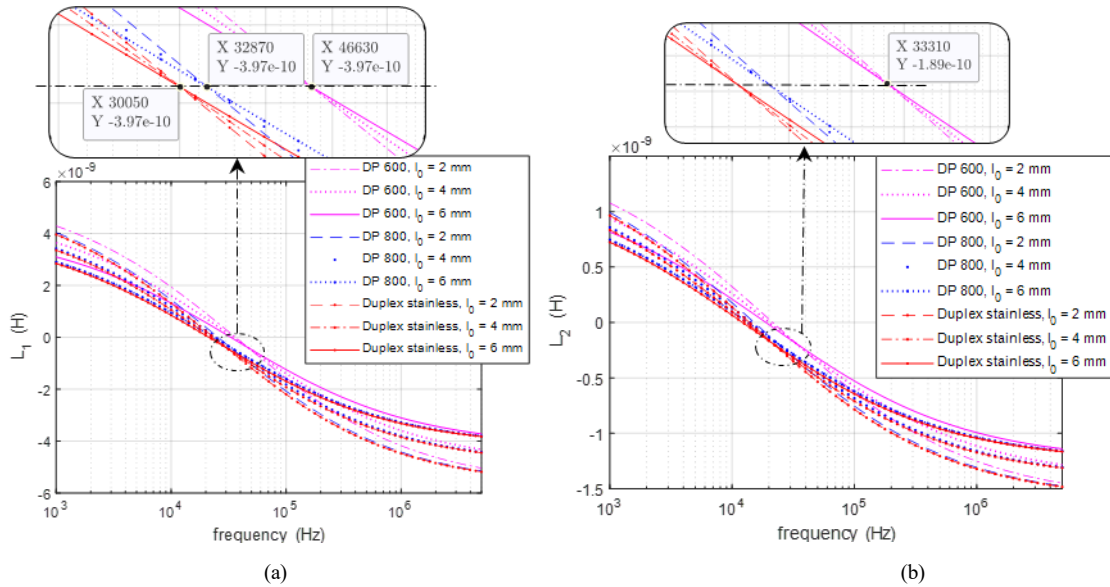
Figure 13 Swept-frequency inductance for the sensor above the magnetic slab with different lift-offs a) transmitter-receiver sensing pair b) transmitter-reference sensing pair (Lu et al.,2021)

1.3.4 Lift-off effect

ECT probes have been proved to efficiently interrogate steel (Meng et al.,2021; Lu et al.,2021). However, the lift-off distance between the probe and metal (particularly for the pancake coil above the metallic slab, as shown in Fig. 5 and Fig. 10) has been found to significantly affect the measured signal, which could further influence the accuracy of inspecting the structural integrity (e.g., surface crack) and measuring the property (e.g., electrical conductivity, magnetic permeability, and thickness) of metallic structures. The lift-off variations can be caused by varying coating thicknesses, irregular sample surfaces, or the operator's movements. The magnetic field is stronger close to the coil and the induced eddy current is stronger when the sample is close to the coil. In many applications, ECT measurements are adversely affected by lift-offs (García-Martín, Gómez-Gil, and Vázquez-Sánchez,2011). In practical measurement, it is not easy to maintain the lift-off spacing between the sample and sensing coils as it commonly varies while moving the sensor or sample. Variations of lift-off could result in significant deviation of sensor signals, which could further lead to overestimated or underestimated results on parameter retrievals. Besides, the sensitivity of sensor signal to lift-off varies under different working frequencies. Therefore, the lift-off is considered a noise source, which is undesirable in both the defect detection and measurement of metallurgical properties.

Various approaches have been proposed to address the lift-off issue on the electromagnetic property measurement of conductive samples, which mainly involves the different sensor designs, measurement techniques, features, and data-processing methods.

Previously, due to the measurement uncertainty of the specimen (for example, the thickness effect; as both the thickness and lift-off can affect the sensor signal), the Lissajous diagram (Theodoulidis,2005) was used for the establishment of a lift-off curve under high frequencies. The method is based on the comparison to calibration specimens. As shown in Fig. 14, a lift-off curve is firstly established at a high frequency (100 kHz for example) using a calibration specimen of nominal thickness. Then, a series of thickness curves are established at a low frequency (1 kHz shown here) at a series of known lift-offs. A multi-frequency measurement is made to first estimate the lift-off from the high frequency, then a corresponding thickness curve is chosen (or interpolated) to apply to the low-frequency measurement, thus determining the thickness. However, the lift-off may vary with different applications (e.g., the influence of surface defect during scanning; eddy current sensor for the real-time monitoring of rail). Additionally, this method requires recalibration for different sensor configurations.
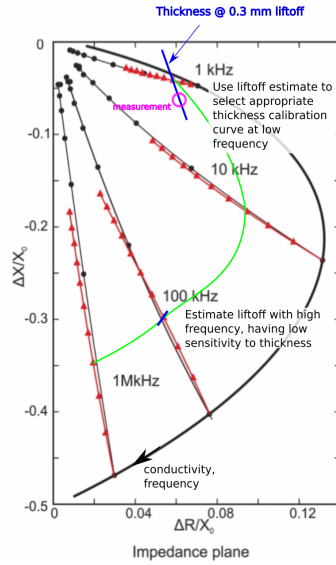
Figure 14 Lissajous diagram; Lift-off in steps of 0.1 mm (triangle) and tilt in steps of 10 degrees (round) for a normalised impedance plane (Theodoulidis,2005)
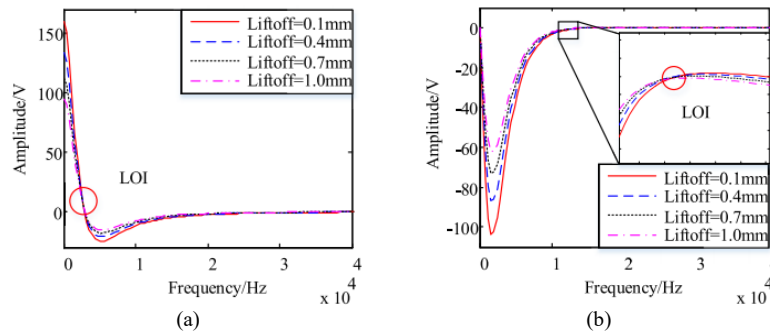
Figure 15 LOI feature of PEC difference signals (a) Real part (b) Imaginary Part (Wen et al.,2019)

For the PEC testing, the point of intersection (LOI) feature (Fig. 15) has been proposed. LOI points result from the invariance of the phase spectrum of PEC responses to lift-off effect, and the time of LOI points would increase with an increase of phase spectrum (Fan et al., 2016). Tian and Sophian used the normalised method with dual signals to further limit the lift-off effect (Tian and Sophian,2005). The LOI feature has been further utilised by researchers to measure the property of the conductive films, multi-layer metallic plates, and steels (Mandache and Lefebvre,2006,; Angani et al.,2016; Wen et al.,2019; Wang et al.,2020).

For the MEC testing, Yin et al. have proposed the peak frequency (PF) and zero-crossing frequency (ZCF) features (As shown in Fig. 16 a) of the MEC inductance spectrum (Fig. 16 b) to reconstruct the thickness of non-magnetic material and ferrite fractions of magnetic alloys (Yin and Peyton,2007; Yin et al.,2009). PF and ZCF of the multi-frequency inductance were found varying with lift-offs, which were used to retrieve the lift-off and parameters using the simplified algorithms (Lu et al.,2017; Lu et al.,2016) deduced from the Dodd-Deeds analytical method (Dodd and Deeds,1968).
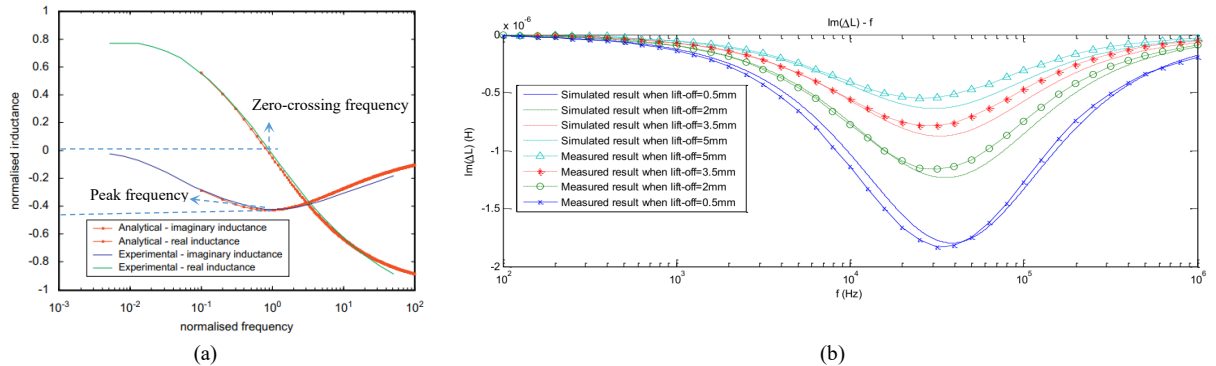
Figure 16 (a) Peak frequency (PF) and zero-crossing frequency (ZCF) features of the MEC spectrum (b) PF feature for non-ferrous materials

(a)

(b)

(c)

(d)
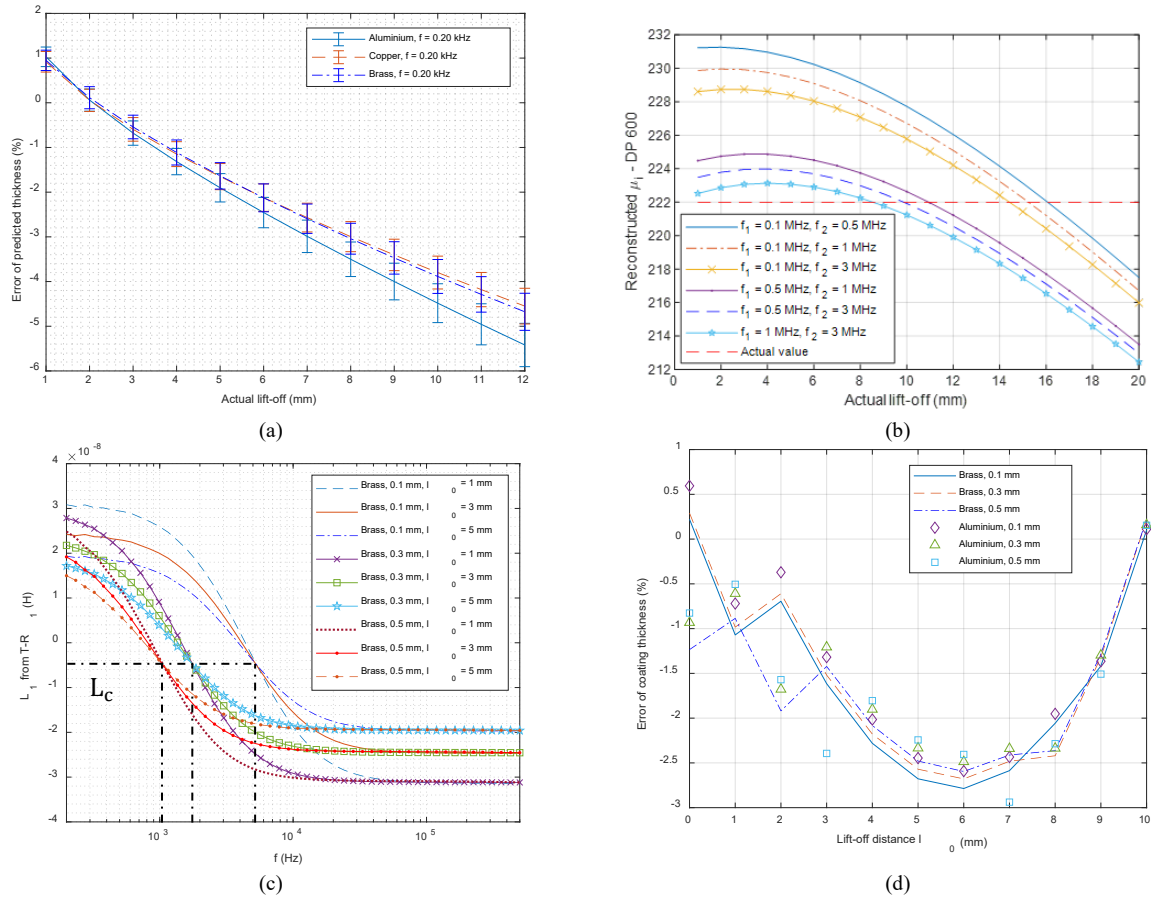
Figure 17 (a) Retrieved thickness of non-ferromagnetic laminates based on the single-frequency quiescent inductance feature (Meng et al.,2021) (b) Retrieved relative permeability of ferromagnetic steels based on the dual-frequency linearity feature of the inductance (Lu et al.,2021) (c) Lift-off insensitive inductance feature for non-ferromagnetic coatings on ferromagnetic substrate (Meng et al.,2021) (d) Relative error of the retrieved coating thickness (Meng et al.,2021)

In my published works, based on the measurement of both single-frequency, dual-frequency, and multi-frequency inductance, various new features and simplified algorithms were used to retrieve the thickness of non-ferromagnetic laminates (Chapter 4) and magnetic permeability (or electrical conductivity) of ferromagnetic slabs (Chapter 3). E.g., for the single-frequency inductance, the method of retrieving thickness of non-ferromagnetic laminates in my published works (Chapter 4.2) is based on a quiescent inductance feature of a single transmitter-receiver probe. Compared to the previous techniques on compensating the retrieval error caused by the lift-off, the lift-off was directly retrieved in my published works. Thus, as Fig. 17 (a) depicts, the relative error of retrieved thickness is less than 6 % for lift-offs up to 12 mm (Meng et al.,2021), which has extended the previous lift-off range (was up to 5 mm) on the thickness retrieval. In my published article (Chapter 3.3), a dual-frequency linearity feature was found on the inductance when using the triple-coil (concentric) probe, which was used to retrieve the magnetic permeability of ferromagnetic steels. In Fig. 17 (b), the lift-off range is extended to 20 mm, while the error of the retrieved permeability is controlled within 4.5 % (Lu et al.,2021). In my published paper (Chapter 5.1) on retrieving the thickness of non-ferromagnetic coatings (on ferromagnetic substrate), a high-frequency quiescent inductance and lift-off insensitive inductance feature (as shown in Fig. 17 (c)) were found on the multi-frequency inductance spectrum (Meng et al. 2021) (for non-ferromagnetic coatings on the ferromagnetic substrate). In Fig. 17 (d), the relative error of the retrieved coating thickness is controlled within 3 % for lift-offs up to 10 mm.

1.3.5 EM computational methods

This research places an emphasis on EM eddy-current computational methods for the efficient simulation of electromagnetic field (and induced eddy currents) and retrieval of the metallic sample properties profile (conductivity, permeability, and thickness) while compensating the lift-off effect.

26

Modelling of ECT (as listed in Table 4) is to simulate the electromagnetic field or calculate the eddy current sensor response (impedance for most cases, or tomographic imaging) for a given sample. In the practical measurement, inhomogeneities may occur in several parameters of the metal, including the defect dimension, magnetic permeability, electric conductivity, geometry of sample (e.g., thickness of the slab), and the lift-off distance between the ECT sensor and test piece. Each of these parameters can affect the detected signals using the ECT sensor. Typically used simulation (or modelling) solvers include analytical formulas and numerical methods.

1.3.5.1 Numerical method

The numerical method of ECT modelling is used for finding the sensor response (impedance or inductance) caused by the defects and metallurgical properties. One of the most used numerical methods of ECT is the A-V form (A for the magnetic vector potential and V for the electric scalar potential) of finite-element (FE) Galerkin equations (Bíró,1999) (the in-depth theory is shown in Chapter 2.1), which was derived from the Maxwell equations with boundary conditions. The FE method of ECT applies to materials of anisotropic properties. Apart from FE methods, the boundary-element (BE) method of ECT has also been applied to defect inspection (Theodoulidis,2010) and magnetic polarization (Lu et al.,2015) of the metal model with uniform or homogenous (or isotropic) properties. The accuracy of the computed result using FE or BE method is dependent on the resolution of discretised mesh. For example, to simulate the sensor response (impedance or inductance) caused by the test piece or the surface notch of steels under high-frequency skin effect, the surface region of steels needs to be finely meshed due to the restrained eddy current near the surface. However, finely discretised mesh models can result in high-rank and highly sparse stiffness matrix (as shown in Fig. 18 c), which leads to hours of cumbersome computations or even divergent results (failure on finding the solution). Thus, more improvements on the numerical methods are needed, which involves the enhancement of fundamental A-V form of FE Galerkin equations, solving strategies and methods.

Improvements on the fundamental equations include the reduced magnetic vector potential (Zeng et al.,2009), optimal preconditioner and diagonalization of stiffness matrix for MEC (as shown in Fig. 18) (Lu, Peyton, and Yin,2017), and the weakly coupled effect (Yin et al.,2018). The FE method of ECT has been used for the retrieval of phase fractions of ferromagnetic steels (Zhou et al.,2018; Davis et al.,2002).

Improvements on solving strategies include a novel decomposition of the model – ParaFEM (Lenzi et al.,2013; Margetts, Leng, and Smith,2006), multi-layered conductive structures (MCS) method (Li, Theodoros, and Tian,2007) and second-order transmission condition (SOTC) techniques approach (Ma and Nie,2013). ParaFEM is a portable library of parallel FE analysis routines that can be used to find the solution of finely discretised subdomains when using the FE method. The principle of this method is decomposing the model into several continuous subdomains and then solving the algebraic equations related to these subdomains in parallel. The method has improved solving efficiency. However, this model has not considered the interactions between the adjacent subdomains. With the MCS method, the computation time was significantly reduced (Li, Theodoros, and Tian, 2007). However, the MCS method can only be used for some layer-isotropic models, such as those encountered in aeroplane and pipeline components, instead of materials with arbitrary geometry (e.g., flawed structures or objects with mixed materials). As an advancement of the finite element domain decomposition method (DDM) in the non-conformal (NC) framework, the SOTC method was proven to be more accurate on computations with iterations over 200, but little improvement for iterations smaller than 50. (Ma and Nie, 2013; Liu and Yuan,2006). The FE-BE hybrid method combines the boundary element region with the finite element region to find solutions for the combinations of isotropic and anisotropic materials (Zhao, Vouvakis, and Lee,2006). This method was well used in most cases except when subdomains are widely separated (Preda et al.,2002; Schrefl et al.,1997).

For improvement of the solving processes, SuiteSparse (Georgii and Westermann,2010) and GRID (Fritschy et al.,2005) were developed to accelerate the solving process of the linear equations in the FE method. The graphics processing unit (GPU) can also accelerate the calculation processes by introducing parallel computing (Godel et al.,2010).
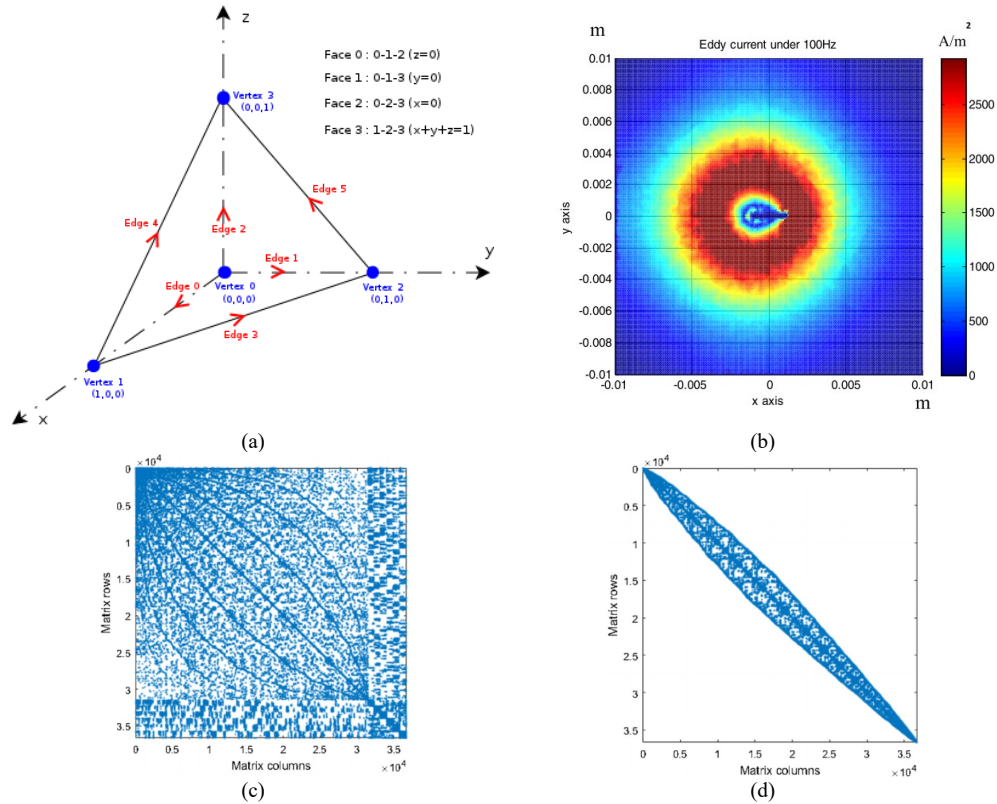
Figure 18 (a) A free tetrahedral mesh subdomain in the edge FE model (b) Simulated eddy current induced (from coils) near the surface of an aluminium foil (Lu, Peyton, and Yin,2017) (c) Sparse stiffness matrix of the FE model (d) Diagonalization of the stiffness matrix (Yin et al.,2018)
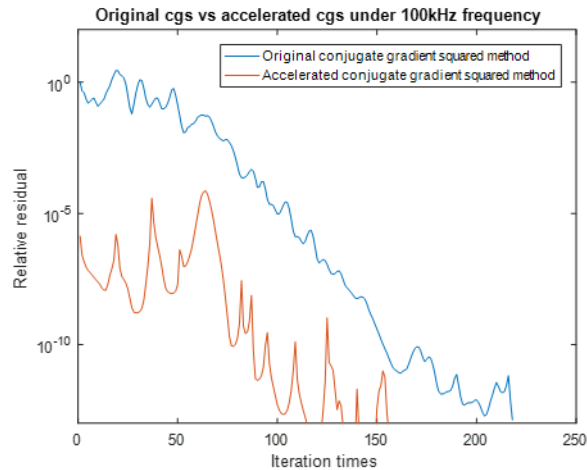
Figure 19 Convergence of original conjugate gradient squared (CGS) method compared with that of conjugate gradient squared (CGS) method with an optimised initial guess (Yin et al.,2018)

In my published article (Chapter 6), a 3D FEM modelling package was developed for the simulation of EM field and sensor impedance (or inductance). The package is able to compute EM simulations for models with over two million overlapping elements. In Fig. 19, compared to commercially available EM simulation software, this package has included an optimised initial guess preconditioning to accelerate the solving process (for the probe scanning process), which has reduced nearly 40 % of the computation time (Yin et al.,2018).

1.3.5.2 Analytical formulas

The analytical formulas are generally efficient than the numerical method as it avoids the cumbersome computations on searching for the solution of the sparse-matrix equations contributed from all the discretised mesh element. Therefore, the analytical method (particularly the simplified version) can apply

to the in situ real-time retrieval of defects and metallurgical properties. Development in the analytical method is needed, particularly the simplification approaches (e.g., most analytical methods are nonlinear and need integration), as it can be used for further real-time retrieval of sample parameters (especially multiple parameters). The Dodd-Deeds analytical model (as shown in Fig. 20 a) has been proposed over a few decades but is still the most dominant method for the problem of an inductive coil above an infinite plate (defect-free) and encircling the infinitely long tube or bar (Dodd and Deeds,1968). An in-depth theory of the Dodd-Deeds analytical solution is presented in Chapter 2.2. To avoid the integration (which is time-consuming, thus making it difficult for the real-time retrieval of material properties), Theodoulidis and Bowler have proposed a truncated region eigenfunction expansion (TREE) method for accelerating the Dodd-Deeds model (Theodoulidis and Bowler,2005). Huang et al. have further revised both the Dodd-Deeds model (Huang et al.,2020) and TREE method for the finite-size disk plates (Huang et al.,2020) (Fig. 20 b), where the boundary of conductive disk slabs is related to the integration limit of wavenumber in the Dodd-Deeds model. Theodoulidis has proposed a tilted version of circular induction coil above the half-space conductor (Theodoulidis,2005) (Fig. 20 c, d).

In my published works (Chapter 3, 4, 5), it was found Bessel series in the integrand of Dodd-Deeds model can be well estimated by sinusoidal functions, which result in a simplified version of model without time-consuming integrations (Meng et al.,2021; Meng et al.,2021; Lu et al.,2021). Besides, in my published article (Chapter 4.5), the Dodd-Deeds analytical formulas were revised to reduce the lift-off effect on the thickness retrieval of the finite-size circular plates (non-ferromagnetic metals) (Lu, Meng et al.,2021). The previous technique on thickness retrieval while reducing the lift-off effect only works for the sample model with infinite planer size (or the planar dimension of sample is at least 5 times of the diameter of probes).

For the analytical model of eddy-current coils inspecting an ideal surface crack, Harfield and Bowler have proposed a thin-skin regime. The proposed regime is valid when the crack length and depth are over 3 to 4 times of the eddy-current skin depth (Harfield and Bowler,1997).

In my published article (Chapter 5.2), a revised thin-skin regime was developed for the mutual impedance of triple-coil driving-pickup eddy current probe scanning over long surface crack with different angles. Based on the revised thin-skin regime of the customed-built probe, the orientation of the surface crack was retrieved with a relative error of 3.5 % (Lu et al.,2021).

However, as most of the analytical solvers are based on the vector potential differential functions (Dodd and Deeds,1968) and boundary conditions of simple geometries (like the half-space, slab, sphere, disk, and cylindrical models), analytical methods are difficult to apply to the modelling of samples (or its components) with complex and irregular geometries (e.g., curved or sawtooth surface notches) (which needs to be calculated by the numerical FEM method – Chapter 1.3.5.1).

The analytical algorithms in my published works were used to embed in the measurement system for the efficient retrieval of sample properties. Overall, the lift-off of eddy-current sensor significantly affects the measured signal (impedance for most cases), and the retrieval of metallurgical properties (conductivity, permeability, and thickness). Previous methods (including novel sensor designs, and features like zero-crossing frequency and peak-frequency feature of MEC and lift-off point of intercept feature of PEC) were used for eliminating the retrieval error caused by the lift-off effect when using the eddy-current sensor. However, these approaches only apply to a small range of lift-off variations (up to 5 mm). In practical measurement, the sensor may have a lift-off of over 10 mm, or even 20 mm in the hot milling applications (the hot-treated samples may damage or influence the probe for lift-offs smaller than 10 mm). Thus, algorithms on property retrieval in my published works have extended the lift-off range (compared to the previous techniques). In my published works, by analysing single-frequency, dual-frequency, or multi-frequency inductance sensitivity (to materials and lift-offs) from single or multiple receiver coils, the retrieval of lift-off range was extended to 10~20 mm. Unlike previous strategies of compensating the lift-off effect (can only compensate the effect of lift-offs up to around 5 mm), the lift-off was directly retrieved prior to the further retrieval of metallurgical properties. With the retrieved lift-off, metallurgical properties (conductivity, permeability, and thickness) of ferromagnetic and non-ferromagnetic steel were obtained based on various probe design (including the triple concentric coils and single transmitter-receiver coil). Moreover, a permeability invariant phenomenon was found for the first time from the inductance-lift-off curve using drive-pickup eddy-current sensors. That is, under the optimal lift-off, the permeability of the test piece barely affects the measured inductance. The developed method was used to decouple the influence

of permeability for the measurement of steel conductivity, which provided a method for metallurgists to non-destructively (in a non-contact manner) evaluate the electrical conductivity when the magnetic permeability of the tested piece is unknown. Details of research contributions are given in Chapter 3, 4, 5, 6.
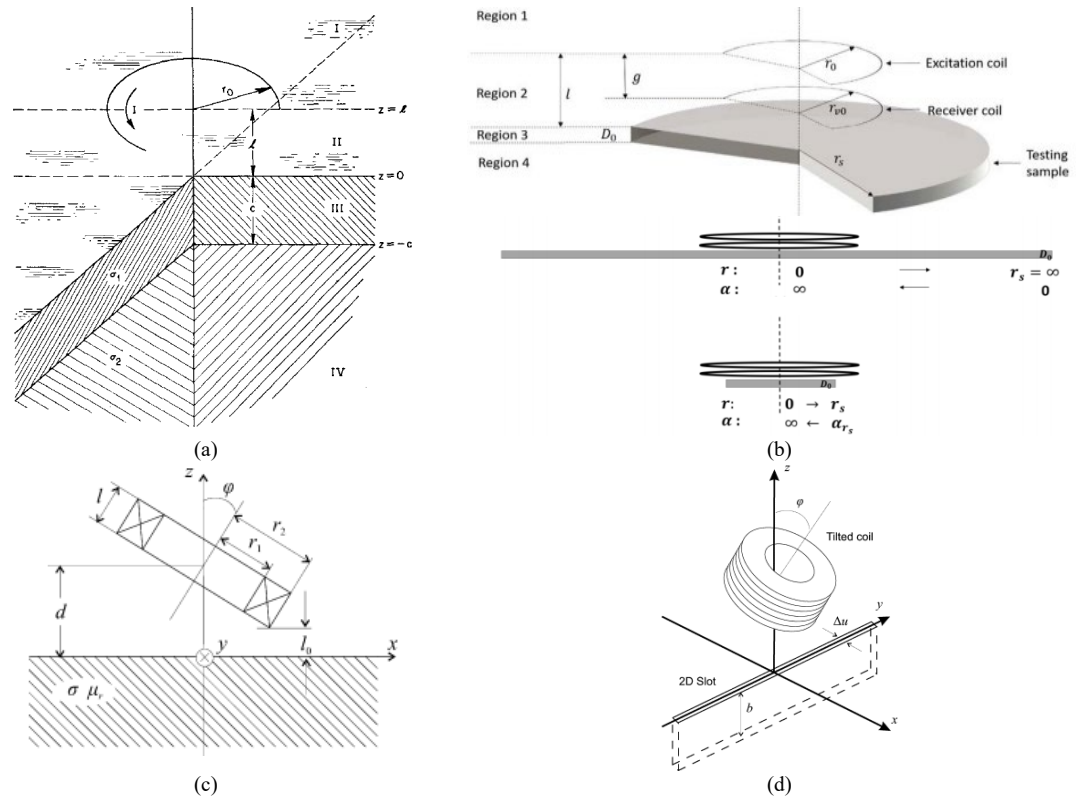
Figure 20 (a) Dodd-Deeds model for an inductive coil above a conductive slab (b) Revised Dodd-Deeds model for conductive disk slabs (Huang et al.,2020) (c) Tilted effect of Dodd-Deeds model (Theodoulidis,2005) (d) Tilted effect of the thin-skin regime (Theodoulidis,2005)

Table 4 Research works on the EM computational methods

Research interest	Research Works
Reduced magnetic vector potential	Zeng et al.,2009
Optimal preconditioner and diagonalization of stiffness matrix (using MEC)	Lu, Peyton, and Yin,2017; My published article in Chapter 6
Weakly coupled effect	Yin et al.,2018
Retrieval of phase fractions	Zhou et al.,2018
ParaFEM	Lenzi et al.,2013; Margetts, Leng, and Smith,2006
Multi-layered conductive structures (MCS) method	Li, Theodoros, and Tian,2007
Second-order transmission condition (SOTC) techniques approach	Ma and Nie,2013; Liu and Yuan,2006
FE-BE hybrid method	Zhao, Vouvakis, and Lee,2006; Preda et al.,2002; Schrefl et al.,1997
SuiteSparse	Georgii and Westermann,2010
GRID	Fritschy et al.,2005
Parallel computing	Godel et al.,2010
Truncated region eigenfunction expansion (TREE) method	Theodoulidis and Bowler,2005; Huang et al.,2020
Derivation of the impedance of a cylindrical coil and the electromagnetic field	Theodoulidis,2005
Thickness of non-ferromagnetic slabs	My published articles in Chapter 4
Electrical conductivity or magnetic permeability of ferromagnetic steels	My published articles in Chapter 3
Thickness of non-ferromagnetic slabs with finite-size circular geometry	My published article in Chapter 4
Thickness of non-ferromagnetic coatings on ferromagnetic substrate	My published article in Chapter 5
Thin-skin regime	Harfield and Bowler,1997
Orientation of surface crack	My published article in Chapter 5

1.4 Thesis outline

This thesis contains 7 chapters. Original manuscripts of the published works related to this study are presented from Chapter 3 to 6 (as listed in Table 5).

Chapter 1 starts with the review of electromagnetic (EM) eddy current testing (ECT). Previous challenges, the improvement and novelty of the research are also included in Chapter 1.

Chapter 2 introduces the background theories used in simulations of EM ECT, including the A-V formed Galerkin equations and the magnetic induction analysis of eddy-current sensor responses based on the Dodd-Deeds formulation. The summary of the achievements, the original contribution, the coherence of published works (in each Chapter), and future works of this study are detailed from Chapter 3 to Chapter 7.

Portfolio of publications

[1] Co-first author * Corresponding author

[1] M. Lu[1], **X. Meng[1]**, W. Yin*, Z. Qu, F. Wu, J. Tang, H. Xu, R. Huang, Z. Chen, Q. Zhao, Z. Zhang, A. Peyton, Thickness measurement of non-magnetic steel plates using a novel planar triple-coil sensor, NDT & E International, vol. 107, pp. 102148, 2019. (Co-first author)

[2] W. Yin[1], **X. Meng[1]**, M. Lu*, Q. Zhao, H. Xu, Z. Zhang, A. Peyton, Permeability invariance phenomenon and measurement of electrical conductivity for ferrite metallic plates, Insight, vol. 61, pp. 472-479, 2019. (Co-first author)

[3] M. Lu, W. Yin*, A. Peyton, Z. Qu, **X. Meng**, Y. Xie, P. Zhao, J. Luo, Q. Zhao, Y. Tao, T. Zhou, Z. Zhang, A model for the triboelectric nanogenerator with inductive load and its energy boost potential, Nano energy, vol. 54, pp. 103883, 2019. (Cover featured article)

[4] W. Yin, M. Lu*, L. Yin, Q. Zhao, **X. Meng**, Z. Zhang, A. Peyton, Acceleration of Eddy Current Computation for Scanning Probes, Insight, vol. 60, pp. 547 – 555, 2018.

[5] L. Yin, B Ye, S. Rodriguez, R. Leiva, **X. Meng**, R. Akid, W. Yin, M. Lu*, Detection of Corrosion Pits Based on an Analytically Optimised Eddy Current Sensor, Insight, vol. 60, pp. 561– 567, 2018.

[6] H. Xu, M. Lu, J. R. Avila, **X. Meng**, W. Yin, Imaging Weld Cross-Section Using a Novel Frequency Feature in Multi-Frequency Eddy Current Testing, Insight, vol. 61, pp.738–743, 2019.

[7] M. Lu,[1]*, **X. Meng[1]**, L. Chen, R. Huang, W. Yin*, A. Peyton, Measurement of ferromagnetic slabs permeability based on a novel planar triple-coil sensor, IEEE Sensors Journal, vol. 20, pp. 2904– 2910, 2020. (Co-first author)

[8] Z. Jin, Y. Meng, R. Yu, R. Huang, M. Lu*, H. Xu, **X. Meng**, Q. Zhao, Z. Zhang, A. Peyton, W. Yin, Methods of Controlling Lift-Off in Conductivity Invariance Phenomenon for Eddy Current Testing, IEEE Access, vol. 8, pp. 122413-122421, 2020.

[9] M. Lu, L. Chen, **X. Meng**, R. Huang*, A. Peyton, W. Yin*, Thickness measurement of metallic film based on a high-frequency feature of triple-coil electromagnetic eddy current sensor, IEEE Transactions on Instrumentation and Measurement, vol. 70, 2021. DOI: 10.1109/TIM.2020.3027929

[10] M. Lu, **X. Meng**, R. Huang, L. Chen, A. Peyton, W. Yin*, Measuring lift-off distance and electromagnetic property of metal using dual-frequency linearity feature, IEEE Transactions on Instrumentation and Measurement, vol. 70, 2021. DOI: 10.1109/TIM.2020.3029348

[11] M. Lu*, **X. Meng**, R. Huang*, L. Chen, A. Peyton, W. Yin*, Lift-off tolerant pancake eddy-current sensor for the thickness and spacing measurement of nonmagnetic plates, IEEE Transactions on Instrumentation and Measurement, vol. 70, 2021. DOI: 10.1109/TIM.2020.3033377

[12] M. Lu*, **X. Meng**, R. Huang*, L. Chen, A. Peyton, W. Yin*, Inversion of distance and magnetic permeability based on material-independent and lift-off insensitive algorithms using eddy current sensor, IEEE Transactions on Instrumentation and Measurement, vol. 70, 2021. DOI: 10.1109/TIM.2020.3036099

[13] **X. Meng,** M. Lu, W. Yin, A. Bennecer*, K. J. Kirk*, Inversion of lift-off distance and thickness for non-magnetic metal using eddy current testing, IEEE Transactions on Instrumentation and Measurement, vol. 70, 2021. DOI: 10.1109/TIM.2020.3038289

[14] M. Lu*, **X. Meng**, R. Huang, J. R. Avila, Z. Chen, L. Chen, A.J. Peyton, W. Yin*, Determination of surface crack orientation based on thin-skin regime using triple-coil drive-pickup eddy-current sensor, IEEE Transactions on Instrumentation and Measurement, vol. 70, 2021. DOI:10.1109/TIM.2020.3044729

[15] M. Lu*[1], **X. Meng[1]**, R. Huang, J. R. Avila, Z. Chen, L. Chen, A. Peyton, W. Yin*, Restoration of surface crack depth for non-magnetic metal from thin-skin imaging using eddy current T-R sensor, IEEE Transactions on Instrumentation and Measurement, in press, 2020.

[16] M. Lu[1], **X. Meng[1]**, R. Huang, L. Chen, A. Peyton, W. Yin*, A high-frequency phase feature for the measurement of magnetic permeability using eddy current sensor, NDT & E International, in press, 2020.

[17] M. Lu*[1], **X. Meng[1]**, R. Huang*, L. Chen, A. Peyton, W. Yin, Thickness measurement of circular metallic film using single-frequency eddy current sensor, NDT & E International, vol. 119, p. 102420, 2021.

[18] M. Lu[1], **X. Meng[1]**, R. Huang, L. Chen, A. Peyton, W. Yin*, Lift-off invariant inductance of steels in multi-frequency eddy-current testing, NDT & E International, in press, 2020.

[19] L. Chen, **X. Meng**, M. Lu*, Q. Ran, X. Liu, W. Yin, Development of a Novel Angle-Sensing Capacitive Sensor with Flexible Electrodes, in press, 2020.

[20] **X. Meng***, M. Lu, W. Yin, A. Bennecer, K.J. Kirk, Evaluation of coating thickness using lift-off insensitivity of eddy current sensor, Sensors, vol 21, no. 2, p. 419, 2021.

Table 5 Corresponding chapters of published works (original manuscripts) in this thesis

Chapter	Published Works
3	"Permeability invariance phenomenon and measurement of electrical conductivity for ferrite metallic plates", Insight, vol. 61, pp. 472-479, 2019 "Measurement of ferromagnetic slabs permeability based on a novel planar triple-coil sensor", IEEE Sensors Journal, vol. 20, pp. 2904– 2910, 2020. "Measuring lift-off distance and electromagnetic property of metal using dual-frequency linearity feature", IEEE Transactions on Instrumentation and Measurement, vol. 70, 2021. 10.1109/TIM.2020.3029348 "Inversion of distance and magnetic permeability based on material-independent and lift-off insensitive algorithms using eddy current sensor", IEEE Transactions on Instrumentation and Measurement, vol. 70, 2021. DOI: 10.1109/TIM.2020.3036099
4	"Thickness measurement of non-magnetic steel plates using a novel planar triple-coil sensor", NDT & E International, vol. 107, pp. 102148, 2019. "Inversion of lift-off distance and thickness for non-magnetic metal using eddy current testing", IEEE Transactions on Instrumentation and Measurement, vol. 70, 2021. DOI: 10.1109/TIM.2020.3038289 "Thickness measurement of metallic film based on a high-frequency feature of triple-coil electromagnetic eddy current sensor", IEEE Transactions on Instrumentation and Measurement, vol. 70, 2021. DOI: 10.1109/TIM.2020.3027929 "Lift-off tolerant pancake eddy-current sensor for the thickness and spacing measurement of nonmagnetic plates", IEEE Transactions on Instrumentation and Measurement, vol. 70, 2021. DOI: 10.1109/TIM.2020.3033377 "Thickness measurement of circular metallic film using single-frequency eddy current sensor", NDT & E International, vol. 119, p. 102420, 2021.
5	"Evaluation of coating thickness using lift-off insensitivity of eddy current sensor", Sensors, vol 21, no. 2, p. 419, 2021. "Determination of surface crack orientation based on thin-skin regime using triple-coil drive-pickup eddy-current sensor", IEEE Transactions on Instrumentation and Measurement, vol. 70, 2021. DOI:10.1109/TIM.2020.3044729
6	"Acceleration of Eddy Current Computation for Scanning Probes", Insight, vol. 60, pp. 547 – 555, 2018.

This thesis presents the published works related to electromagnetic eddy-current computational methods for the simulation (modelling) of electromagnetic field (and induced eddy currents) and reconstruction (retrieval) of the metallic sample properties profile (conductivity, permeability, and thickness) while compensating the lift-off effect.

Several features using the simplified Dodd-Deeds formula were found for the retrieval of metallurgical properties (electrical conductivity, magnetic permeability, and thickness) while reducing the lift-off effect (Chapter 3, 4, 5). Besides, a revised thin-skin regime was used to determine the orientation of surface crack on ferromagnetic steels (Chapter 5). An acceleration method was developed to hasten the numerical FE model (Chapter 6), particularly for the eddy-current probes laterally scanning over the surface flaw.

Chapter 2 Background theories

2.1 Finite edge-element method for the electromagnetic eddy current testing

In this section, the fundamental formulations for the conventional discretised boundary edge-element method – A-V form Galerkin equations is presented. A-V form Galerkin equations have been formulated over two decades and are still the most dominant formulation for the general calculations of the electromagnetic field (Bíró,1999).

2.1.1 A-V form Galerkin equations – boundary element analysis

1) Derivations of A-V form Galerkin equations

In the non-conducting region Ω_n, according to Ampère's circuital law

$$\nabla \times \mathbf{B}_s = \frac{\mathbf{J}_0}{v_0} \tag{5}$$

Similarly, for the conductive region Ω_c

$$\nabla \times \mathbf{B} = \frac{\mathbf{J}}{v} \tag{6}$$

$$\nabla \cdot \mathbf{E} = 0 \tag{7}$$

v_0 and v are the reluctivity (the reciprocal of the permeability) of the free space and conductive material. $\mathbf{J}_0$ is the current density of the excitation source. $\mathbf{B}_s$ and $\mathbf{B}$ are the magnetic flux density of the free space and within the material. $\mathbf{E}$ is the electric field within the material.

$\mathbf{J}$ is the induced eddy current within the material, which follows the constitutive equation.

$$\mathbf{J} = \sigma\mathbf{E} \tag{8}$$

σ is the electrical conductivity.

Combine (6) and (8)

$$v\nabla \times \mathbf{B} = \sigma\mathbf{E} \tag{9}$$

The magnetic vector potential in the free space $\mathbf{A}_s$ and within the material $\mathbf{A}$ are defined as

$$\mathbf{B} = \nabla \times \mathbf{A} \tag{10}$$

$$\mathbf{B}_s = \nabla \times \mathbf{A}_s \tag{11}$$

$$\mathbf{E} = -j\omega\mathbf{A} - j\omega\nabla V \tag{12}$$

V is the electric scalar potential within the material.

Combine (9) with (10) and (11), and (7) with (12) in the conductive region Ω_c

$$v\nabla \times (\nabla \times \mathbf{A}) + j\omega\sigma\mathbf{A} + j\omega\sigma\nabla V = \mathbf{0} \tag{13}$$

$$\nabla \cdot (j\omega\mathbf{A} + j\omega\nabla V) = 0 \tag{14}$$

According to the boundary condition of the magnetic field intensity $\mathbf{H} = v\mathbf{B}$ and $\mathbf{B}$, $\mathbf{H} \times \mathbf{n}$ and $\mathbf{B} \cdot \mathbf{n}$ are continuous at the material interface ($\mathbf{n}$ is the outer normal unit vector). Therefore, the Dirichlet and Neumann boundary conditions of the vector potential $\mathbf{A}$ (referring equation 14) and scalar potential V (referring equation 9 and 12) at the material interface are

$$(\nabla \times \mathbf{A}) \times \mathbf{n} = (\nabla \times \mathbf{A}_s) \times \mathbf{n} \tag{15}$$

$$(-j\omega\mathbf{A} - j\omega\nabla V) \cdot \mathbf{n} = 0 \tag{16}$$

2) General formulas

The mesh domain with anisotropic material properties (v and σ) can be discretised into finite subdomains. Assuming subdomains are with tetrahedral geometry (with 6 edges and 4 vertex nodes), for each subdomain (e.g., n^{th} subdomain element), the magnetic vector potential is approximated by the edge basis function.

$$\mathbf{A} \approx A^{(n)} = \sum_{i=1}^{6} a_i \mathbf{N}_i \tag{17}$$

a_i is the line integral of A along i^{th} edge of each subdomain. $\mathbf{N}_i$ denotes the edge basis function for the interpolation of the magnetic vector potential on i^{th} edge.

Similarly, the electric scalar potential for each subdomain can be approximated by the nodal basis function.

$$V \approx V^{(n)} = \sum_{j=1}^{4} V_j L_j \tag{18}$$

V_j is the electric scalar potential of jth vertex node. L_j denotes the nodal basis function for the interpolation of the electric scalar potential on j^{th} vertex node.

Combine (13) and (14) with (Dirichlet and Neumann) boundary conditions (15) and (16), and basis functions (17) and (18), the following Galerkin equations are derived (Bíró,1999).

$$\int_{\Omega_c} \nabla \times \mathbf{N}_i \cdot v^{(n)} \nabla \times \mathbf{A}^{(n)} d\Omega + \int_{\Omega_c} j\omega\sigma^{(n)} \mathbf{N}_i \cdot \mathbf{A}^{(n)} d\Omega + \int_{\Omega_c} j\omega\sigma^{(n)} \mathbf{N}_i \cdot \nabla V^{(n)} d\Omega =$$
$$\int_{\Omega_c} \nabla \times \mathbf{N}_i \cdot v_0 \nabla \times \mathbf{A}_s d\Omega \ , i = 1, 2, \dots, 6 \tag{19}$$

$$\int_{\Omega_c} j\omega\sigma^{(n)} \nabla L_i \cdot \mathbf{A}^{(n)} d\Omega + \int_{\Omega_c} j\omega\sigma^{(n)} \nabla L_i \cdot \nabla V^{(n)} d\Omega = 0 \ , j = 1, 2, \dots, 4 \tag{20}$$

Equation (19) controls the generation of the dynamic electromagnetic fields, including the generation the main waveform of magnetic vector potential (first term), the diffusion or the skin effect factor (second term), and the Maxwell Wagner effect (third term, i.e., the geometry of the sample affects the electric scalar potential of the vertex).

Equation (20) determines the generation of the static electromagnetic fields.

The original A-V form Galerkin equations can be transformed into matrix form, as shown in the following.

$$\sum_{n=1}^{N_0} \begin{pmatrix} K_1^{(n)} + K_2^{(n)} & L^{(n)} \\ M^{(n)} & N^{(n)} \end{pmatrix} \cdot \begin{pmatrix} \mathbf{A}^{(n)} \\ V^{(n)} \end{pmatrix} = B \tag{21}$$

In equation (21), $K_1^{(n)}$ and $K_2^{(n)}$ denote the matrix form of the first and second term in equation (19). $L^{(n)}$ is the matrix form of the third term in equation (19). $M^{(n)}$ is the matrix form of the first term in equation (20). $N^{(n)}$ is the matrix form of the second term in equation (20). B is the matrix form of the right-hand side of equation (19), contributing to the generations of the background field. The stiffness matrix is composed of $K^{(n)}$, $L^{(n)}$, $M^{(n)}$, and $N^{(n)}$, which determines the field solution of the nth subdomain element - magnetic vector potential $\mathbf{A}^{(n)}$ and electric scalar potential $V^{(n)}$. N_0 is the total number of discretised subdomains.

2.1.2 Evaluation of the background field

The background B matrix in (21) is

$$B = \begin{bmatrix} \int_{\Omega_c} \nabla \times \mathbf{N}_i \cdot v_0 \nabla \times \mathbf{A}_s d\Omega \\ 0 \end{bmatrix} \tag{22}$$

34

In equation (22), O is a null matrix vector. The length of the vector O equals that of matrix vector V, which is the total number of the vertex for the whole mesh element subdomains. The background magnetic vector potential $\mathbf{A}_s$ can be calculated by using the Biot-Savart law:

$$\mathbf{A}_s = \frac{\mu_0 I_0}{4\pi} \int_c \frac{d\boldsymbol{l} \times \hat{\mathbf{r}}}{|r|} \tag{23}$$

In equation (23), $d\boldsymbol{l}$ denotes the unit vector of the current segment. For the current flowing in a circular coil, $d\boldsymbol{l}$ is the differential element vector of the coil segment. I_0 denotes the current in the coil. μ_0 is the permeability of the free space. r is the distance between the current segment and the point for the field to be calculated. $\hat{\mathbf{r}}$ is the unit vector directing from current segment to the point.

2.1.3 Calculation of electric field and eddy current distributions

The electric field of nth subdomain element can also be derived from the vector potential $\mathbf{A}^{(n)}$ and electric scalar potential $V^{(n)}$ in equation (21) by referring to the derivative of the Coulomb gauge (Zeng et al,2009):

$$\mathbf{E}^{(n)} = -j\omega\mathbf{A}^{(n)} - j\omega\nabla V^{(n)} \tag{24}$$

Further, the eddy current distributions can be derived via Ohm's law:

$$\mathbf{J}^{(n)} = \sigma^{(n)}\mathbf{E}^{(n)} \tag{25}$$

2.1.4 Induced voltage and mutual impedance/inductance of the transmitter-receiver

Therefore, the induced voltage and the transmitter-receiver mutual impedance or inductance with the presence of the sample can also be obtained by referring to the equation proposed by Mortarelli (1980), Auld and Moulder (1999). In both methods, the authors start from the Lorentz reciprocity relation and arrive at the same generalized equation that can be applied to any pair of coils,

$$V_c = \frac{1}{I_0} \int_c \mathbf{E}_a \cdot \mathbf{J}_b \, dC = \frac{1}{I_0} \int_c \mathbf{E}_a \cdot \mathbf{E}_b \cdot (\sigma_a - \sigma_b) dC \tag{26}$$

$$L = \frac{1}{j\omega I_0{}^2} \int_c \mathbf{E}_a \cdot \mathbf{J}_b \, dC = \frac{1}{I_0{}^2} \int_c \mathbf{E}_a \cdot \mathbf{E}_b \cdot (\sigma_a - \sigma_b) dC \tag{27}$$

Here, V_c, L denotes the induced voltage and mutual inductance on the transmitter-receiver sensing pair caused by the difference between medium a and b. C denotes the conductive region.

2.1.5 Investigation of contributions from each term of Galerkin equations on the generation of the electromagnetic field

1) $K_1{}^{(n)}$- basic wave generation

$K_1{}^{(n)}$, the first term in equation (19) controls the generation of the fundamental magnetic vector potential. To investigate how $K_1{}^{(n)}$ affect the solution of $\mathbf{A}^{(n)}$ and eddy currents, as equation (28) and (29) depict, a conductive sphere model is built for the simulation of the magnetic vector potential. Models with a regular (symmetric with respect to the axis of coils) geometries can be used to replace the sphere for simulations, as long as the symmetry of induced eddy currents is not affected by the boundary of objects.

$$\sum_{n=1}^{N_0} K_1{}^{(n)} \cdot \mathbf{A}^{(n)} = B \tag{28}$$

Since the coil is co-axially located above the sphere model, the gradient of the scalar potential $\nabla V^{(n)}$ is neglectable especially around the centre of the sphere. Then, the eddy current in a deep x-y plane can be calculated as

$$\mathbf{J}^{(n)} = \sigma^{(n)}\mathbf{E}^{(n)} = -j\omega\sigma^{(n)}\mathbf{A}^{(n)} \qquad (29)$$
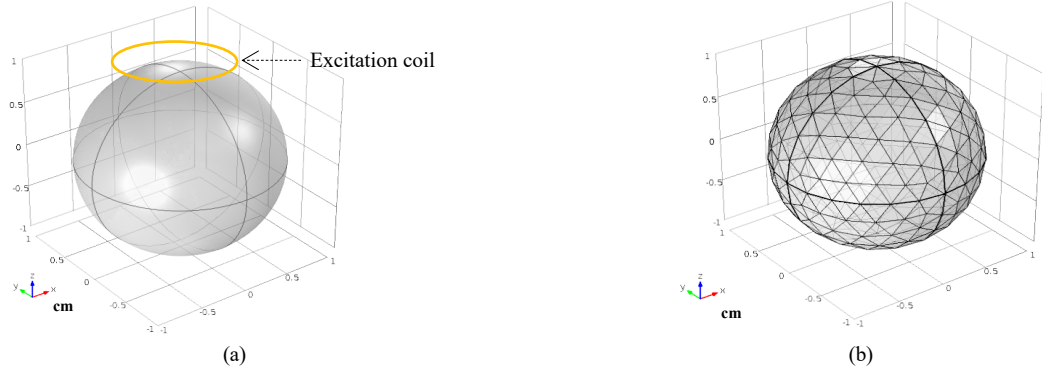
Figure 21 (a) Aluminium sphere model a) model domain b) discretised into subdomain mesh elements

In Fig. 21 a), an aluminium sphere model with an electrical conductivity of 35 MS/m and radius of 1 cm is built. An excitation coil with a radius of 0.5 cm and unit ampere flowing current is co-axially located on the top of the sphere. The distance between the centre of coil and sphere is 1.2 cm. The working frequency of the excitation current is 200 kHz. The sphere model domain in Fig. 21 a) is discretised into subdomain mesh (tetrahedral) elements via COMSOL. The computation can be operated by the COMSOL integrated solver. Alternatively, the mesh information including the sequence of the subdomains, vertex coordinates of each tetrahedral subdomain, and properties (electrical conductivity and magnetic permeability), can be loaded by MATLAB for the further calculation via equation (28). Since the modified equations used in (28) are different from (only one factor or term of) the fundamental equations (in COMSOL based solver), computations are operated via MATLAB. Besides, with the MATLAB custom scripted solver (using BiCGSTAB technique), the computation can be further accelerated by the diagonalization (reordering and decomposing) of the ill-posed stiffness matrix with the optimization of the initial preconditioner for both adjacent scanning probe positions (Yin et al,2018) and frequencies (Lu, Peyton, and Yin,2017). Moreover, with the MATLAB scripted solver, the computation can be further hastened by calling GPU functions or using the simplified function based on the weakly-coupled effect (Yin et al,2018). The background field in matrix B is calculated via the Biot-savart law in (22) and (23). Finally, the eddy current contributed by the first term of Galerkin equation (19) – $K_1^{(n)}$ matrix is calculated via equation (29).
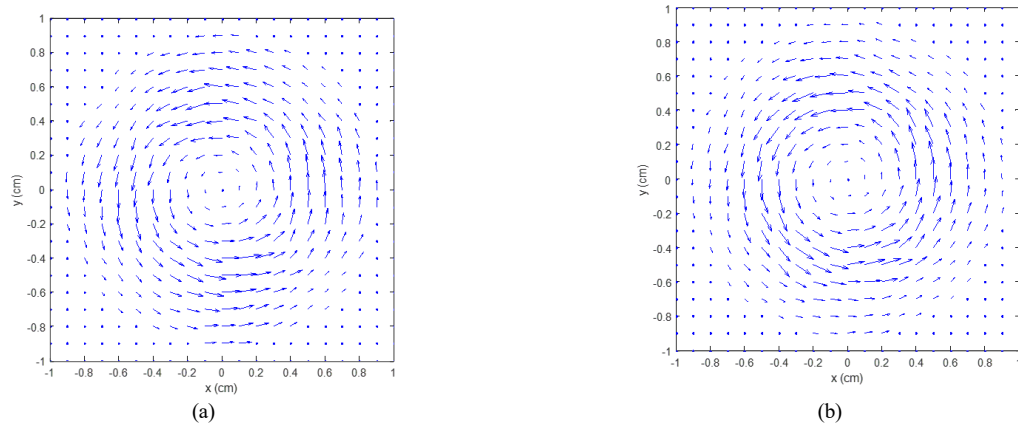
Figure 22 Eddy current contributed by $K_1^{(n)}$ matrix a) depth of z = 0 cm b) depth of z = 0.2 cm

The eddy current (contributed by $K_1^{(n)}$) quiver maps in x-y planes at the depth of z = 0 cm and z = 0.2 cm are illustrated in Fig. 22. It can be observed from Fig. 22 (b) that the largest eddy current is distributed on radius of 0.5 cm (the same radius of the excitation coil). Moreover, as Fig. 22 (a) depicts, the eddy current is slightly dispersed from radius of 0.5 cm. This is because the x-y plane at z = 0 cm is farther than that at z = 0.2 cm, which affects the distribution of eddy currents (the eddy current decays) with depth. In general, the eddy current contributed by $K_1^{(n)}$ mainly follows the geometry and location of the excitation coil.

36

2) $K_2^{(n)}$- Skin or diffusion effect

The skin or diffusion effect is a tendency that the eddy current become weaker with depth. Empirically, the eddy current is mainly distributed underneath the surface of the conductor at high frequencies. As depicted in Fig. 23, to investigate the eddy current skin effect, a circular coil is co-axially and parallelly deployed on an Aluminium cylinder. The top of object is modelled as plane surface so that the eddy current can be efficiently analysed in different layers of depth. Models with alternative geometries (e.g., plate) can also be used for simulations, as long as the induced eddy current is axially symmetric (to coils) and comparable between different layers of depth. The eddy current skin effect is due to the restraint of the magnetic field excited by the varying current flowing in the coil under high frequencies. In Fig. 23 and 24, the model is an aluminium (electrical conductivity of 35 MS/m) cylinder with a diameter and height of 1 cm. The diameter of the excitation coil is 0.2 mm. The coil with the flowing current of unit ampere is co-axially deployed above the aluminium cylinder (with a small lift-off of 0.2 cm).
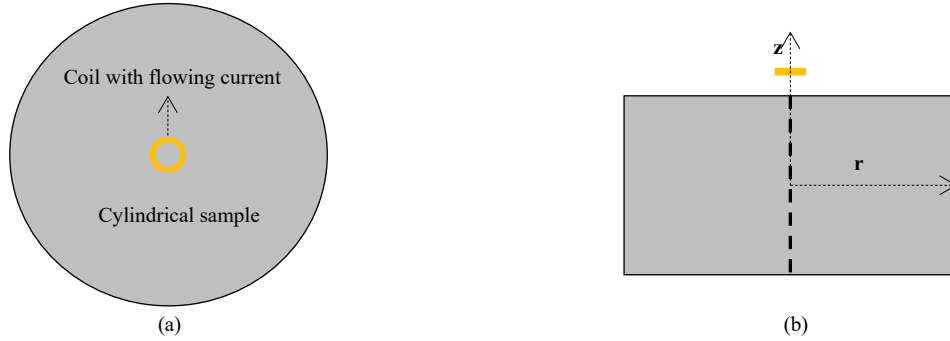
Figure 23 Analysis of eddy current skin effect for a coil above a cylindrical sample a) top view b) front view

The skin depth of the eddy current is determined by both the working frequency of the excitation current, the electrical conductivity and the magnetic permeability of the sample, which can be calculated via equation (30).

$$\delta = \sqrt{\frac{2}{\omega \sigma \mu_r \mu_0}} \tag{30}$$

μ_r and μ_0 are the relative and vacuum magnetic permeability for the sample and free space.

To analyse the behaviour of the eddy current skin effect, the magnetic vector potential can be derived via equation (31). The eddy current is computed from equation (32).

$$\sum_{n=1}^{N_0} K_2^{(n)} \cdot \mathbf{A}^{(n)} = \mathrm{B} \tag{31}$$

$$\mathbf{J}^{(n)} = \sigma^{(n)} \mathbf{E}^{(n)} = -j\omega\sigma^{(n)}\mathbf{A}^{(n)} - j\omega\sigma^{(n)}\nabla V^{(n)} \tag{32}$$

Figure 24 Aluminium cylinder model

The operation frequency of the excitation current are 1 MHz and 4 MHz. The model was discretised into tetrahedral subdomains via COMSOL and exported into MATLAB for the eddy current computation from equation (32).

(a)

(b)
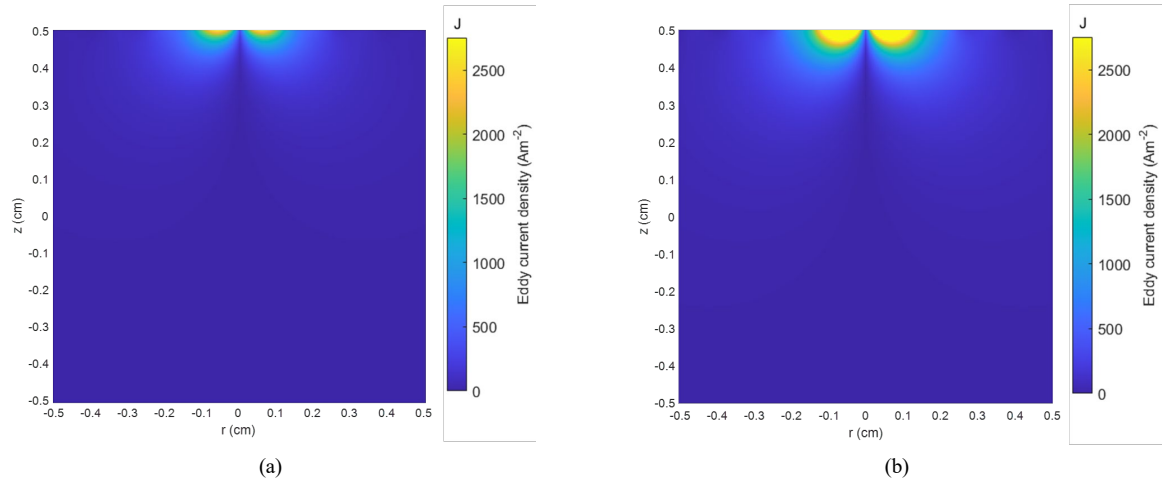
Figure 25 Cross-section eddy current scattering (in r-z plane) contributed by $K_2^{(n)}$ matrix a) working frequency of 1 MHz b) working frequency of 4 MHz

Fig. 25 demonstrates the eddy current scattering in r-z plane under the working frequencies of 1 MHz and 4 MHz. It can be observed the eddy current attenuates faster at high frequencies with increasing depth. Since the eddy current is restrained underneath the surface of the sample, the mesh domain area around the skin of the sample needs to be finer discretised under high frequencies.

3) $L^{(n)}$- Maxwell Wagner effect

The third term of Galerkin equation (19), i.e., $L^{(n)}$ in equation (21) illustrates how the magnetic vector potential field and eddy current are affected by the geometry of the sample (or inhomogeneities of the material properties) – the Maxwell Wagner effect. A model has been built for the analysis of eddy currents contributed by matrix $L^{(n)}$.
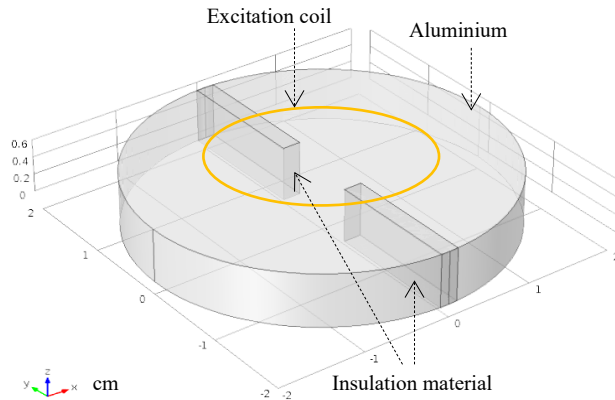
Figure 26 Aluminium pie model for the analysis of eddy current contributed by matrix $L^{(n)}$

In Fig. 26, the excitation coil (with a diameter of 2 cm and flowing current of 1 Ampere under working frequency of 200 kHz) is co-axially deployed above (with a lift-off of 0.1 cm) a pie (cylindrical plate) sample. The pie sample is composed of aluminium (with an electrical conductivity of 35 MS/m) and two insulation interfaces (width of 0.1 cm, length of 1.5 cm). The radius and thickness of the pie sample are 2 cm and 0.6 cm. The model is used to investigate how the materials inhomogeneities affect the field and eddy current distributions.
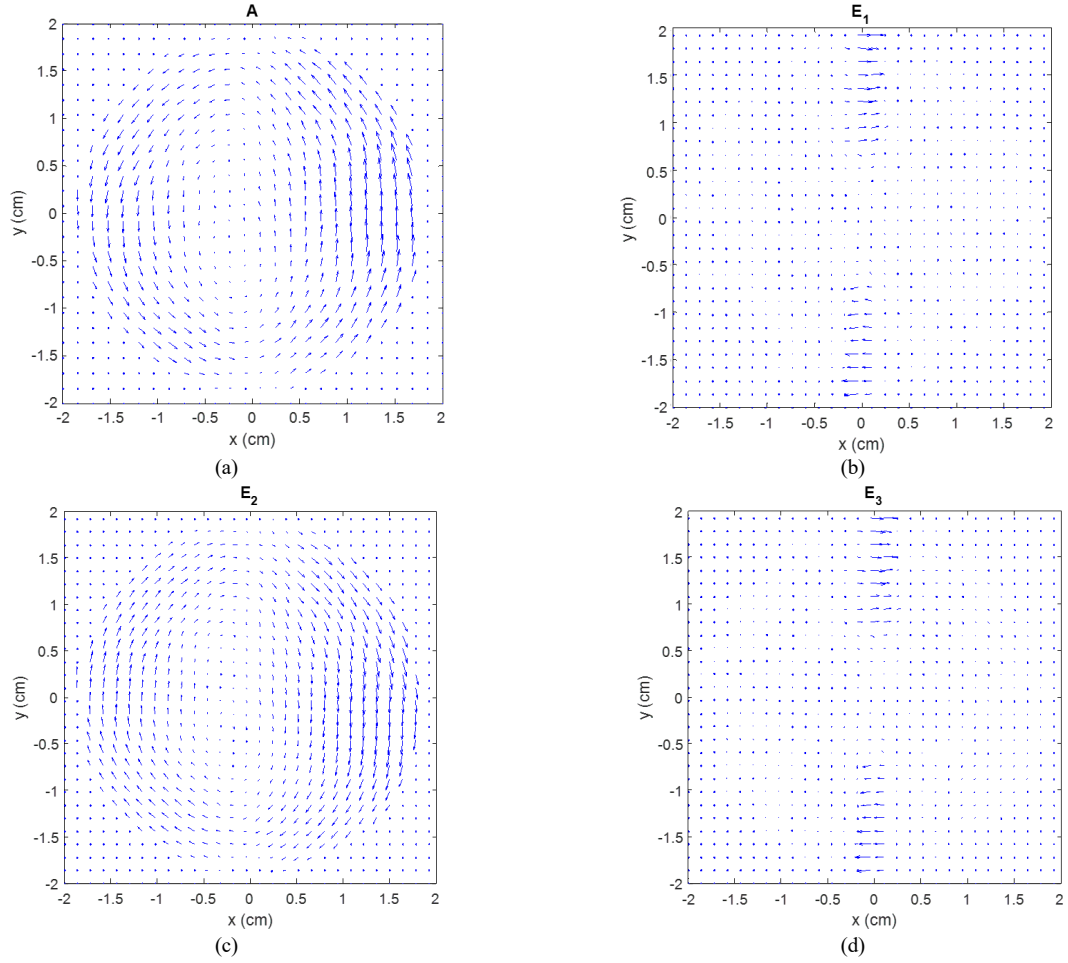
Figure 27 Result of the pie model in x-y plane at z = 0.3 cm a) magnetic vector potential $\mathbf{A}^{(n)}$ b) electric field contributed by the gradient of electric vertex scalar potential $\left(\mathbf{E}_1^{(n)} = -j\omega\nabla V^{(n)}\right)$ c) electric field contributed by the magnetic vector potential $\left(\mathbf{E}_2^{(n)} = -j\omega\mathbf{A}^{(n)}\right)$ d) electric field contributed by both the magnetic vector potential and gradient of the electric vertex scalar potential $\left(\mathbf{E}_3^{(n)} = -j\omega\mathbf{A}^{(n)} - j\omega\nabla V^{(n)}\right)$

In Fig. 27 (a), the magnetic vector potential $\mathbf{A}^{(n)}$ is calculated by equation (21), which is contributed by both matrices $K_1^{(n)}$ and $K_2^{(n)}$. It can be observed that the $\mathbf{A}^{(n)}$ field around the insulation area is weaker than that in the aluminium area, which is due to the contributions of matrix $K_2^{(n)}$. Fig. 27 (b) illustrates the electric field $\mathbf{E}_1^{(n)}$ contributed by the gradient of electric vertex scalar potential $-j\omega\nabla V^{(n)}$. The electric field $\mathbf{E}_1^{(n)}$ is mainly generated by the electric scalar $V^{(n)}$ different between the two interfaces of the insulation block, which is much larger than the electric field $\mathbf{E}_2^{(n)}$ contributed by the magnetic vector potential $-j\omega\mathbf{A}^{(n)}$. Therefore, as shown in Fig. 27 (d), the overall electric field $\mathbf{E}_3^{(n)}$ contributed by both the magnetic vector potential and gradient of the electric vertex scalar potential $\left(-j\omega\mathbf{A}^{(n)} - j\omega\nabla V^{(n)}\right)$ is almost the same as the electric field $\mathbf{E}_1^{(n)}$.

(a)   (b)

(c)   (d)
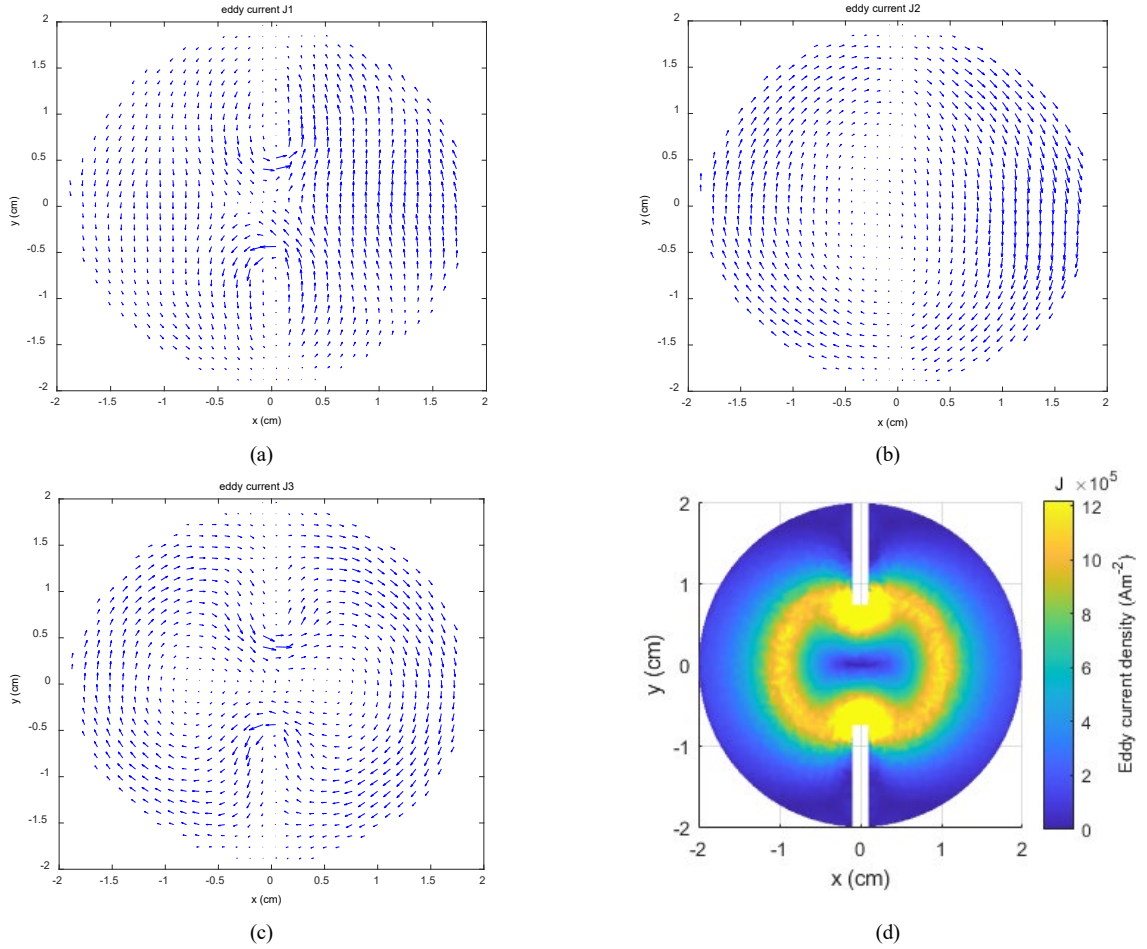
Figure 28 Result of the pie model in x-y plane at z = 0.3 cm a) eddy current contributed by the gradient of electric vertex scalar potential $\left(\mathbf{J}_1^{(n)} = \sigma^{(n)}\mathbf{E}_1^{(n)} = -j\omega\sigma^{(n)}\nabla V^{(n)}\right)$ b) eddy current contributed by the magnetic vector potential $\left(\mathbf{J}_2^{(n)} = \sigma^{(n)}\mathbf{E}_2^{(n)} = -j\omega\sigma^{(n)}\mathbf{A}^{(n)}\right)$ c) overall eddy current contributed by both the magnetic vector potential and gradient of the electric vertex scalar potential $\left(\mathbf{J}_3^{(n)} = \sigma^{(n)}\mathbf{E}_3^{(n)} = -j\omega\sigm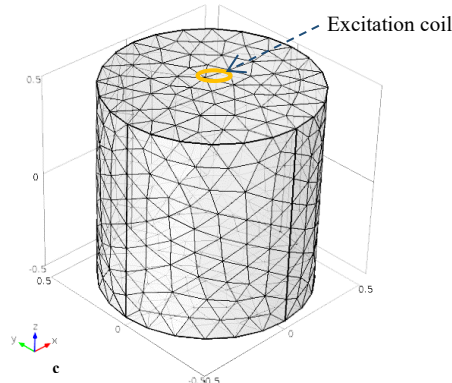a^{(n)}\mathbf{A}^{(n)} - j\omega\sigma^{(n)}\nabla V^{(n)}\right)$ d) colormap of the eddy current density at z = 0.3 cm

Fig. 28 a b and c depict the eddy current quiver maps contributed by electric field $\mathbf{E}_1^{(n)}$, $\mathbf{E}_2^{(n)}$, and $\mathbf{E}_3^{(n)}$. Fig. 28 d illustrates the eddy current density contributed by $\mathbf{E}_3^{(n)}$ at z = 0.3 cm. By combing both eddy current contributions ($-j\omega\sigma^{(n)}\mathbf{A}^{(n)}$ from both magnetic vector potential and $-j\omega\sigma^{(n)}\nabla V^{(n)}$ from the gradient of electric vertex scalar potential), the overall eddy current follows the coils route but is restrained by the insulation interfaces.

Overall, in the A-V form Galerkin equations, different terms in (21) control the generations of both dynamic and static electromagnetic fields, which have considered the effect of coils, frequencies of excitation currents, and properties of media (subdomains) or geometries of objects.

2.2 Magnetic induction analysis based on Dodd-Deeds formulation

The above section (2.1) focuses on the electromagnetic simulation using finite element method (FEM), which applies to any kinds of media (e.g., objects with anisotropic properties). However, cumbersome computations are needed due to the sparse stiffness matrix when using the FEM, which takes hours of calculations and even results in divergence (cannot find the solution). Besides, the FEM method cannot efficiently and accurately apply to the high-frequency and scanning probe simulations, which need extremely fine surface mesh and re-discretise the whole object in each frequency or coil position step.

For the test piece with symmetric geometry and properties, analytical formulas are commonly used as they are more efficient than the FEM numerical modelling. Dodd-Deeds analytical formulas have been proposed for decades, which is still the dominant and general analytical solution for the calculation of a circular coil above a metallic plate (or cylindrical rod) (Dodd and Deeds, 1968). The Dodd-Deeds formulas only apply to half-space or axially (coil) symmetric objects like disk plates and cylinders.
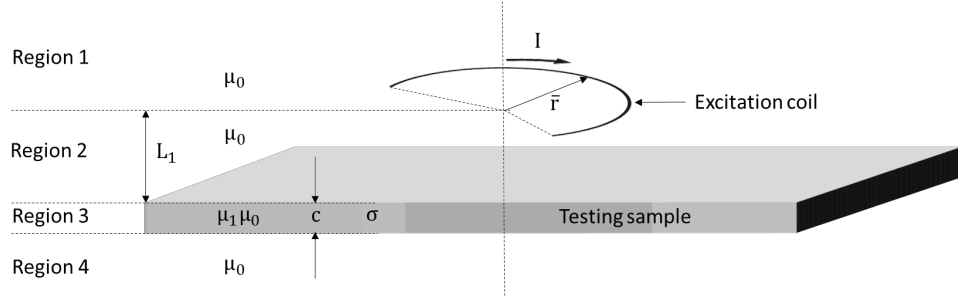
Figure 29 Division of the region for a circular coil above a metal plate

As Fig. 29 depicts, the entire domain for a coil above a sample is divided into four regions. The differential equations in the region 1, 2, 4 (air) and 3 (metallic sample) are

$$\partial^2 A/\partial r^2 + (1/r)\,\partial A/\partial r + \partial^2 A/\partial z^2 - A/r^2 = 0 \tag{33}$$

$$\partial^2 A/\partial r^2 + (1/r)\,\partial A/\partial r + \partial^2 A/\partial z^2 - A/r^2 - j\omega\mu_1\mu_0\sigma A = 0 \tag{34}$$

Where, r and z are the variables in spherical coordinate system. A is the magnitude of the magnetic vector potential. From the Dodd and Deeds (1968) method, by combining the boundary conditions on the interfaces between the domain regions, the solution of the magnetic vector potential in region 1 and 2 is shown as follows.

$$A_{1,2}(r,z) = \frac{NI\mu_0}{2(L_2 - L_1)(r_2 - r_1)}\int_0^\infty \frac{P(\alpha)J_1(\alpha)}{\alpha^3}Y(\alpha)\,d\alpha \tag{35}$$

$$Y(\alpha) = 2 - e^{\alpha(z-L_2)} - e^{\alpha(z-L_1)} + -e^{-\alpha z}\big(e^{-\alpha L_1} - e^{-\alpha L_2}\big)\phi(\alpha) \tag{36}$$

$$P(\alpha) = \int_{\alpha r_1}^{\alpha r_2} \tau J_1(\tau)\,d\tau \tag{37}$$

$$\phi(\alpha) = \frac{(\alpha_1 + \mu_1\alpha)(\alpha_1 - \mu_1\alpha) - (\alpha_1 + \mu_1\alpha)(\alpha_1 - \mu_1\alpha)e^{2\alpha_1 c}}{-(\alpha_1 - \mu_1\alpha)(\alpha_1 - \mu_1\alpha) + (\alpha_1 + \mu_1\alpha)(\alpha_1 + \mu_1\alpha)e^{2\alpha_1 c}} \tag{38}$$

$$\alpha_1 = \sqrt{\alpha^2 + j\omega\sigma\mu_1\mu_0} \tag{39}$$

Where, r_1, and r_2 are the inner and outer radii of the transmitter coil. ω is the working angular frequency. N denotes the turns of the transmitter coil. μ_0 is the vacuum permeability. μ_1, c, and σ are the relative permeability, and electrical conductivity of the metallic sample. L_1 is the lift-off or the lower height of the transmitter coil. L_2 is the upper height of the transmitter coil. J_1 is the first order Bessel function of the first kind. τ and α denote the integrated parameters.

The receiver coil is deployed coaxially next to the transmitter coil. After getting the magnetic vector potential, the induced voltage between the transmitter and receiver coil can be derived by integrating it over the cross-section of the receiver coil, as shown in Equation (40).

$$V = \frac{j2\pi\omega N'}{(L_2' - L_1')(r_2' - r_1')} \int_{L_1'}^{L_2'} \int_{r_1'}^{r_2'} rA_{1,2}(r,z)\, dr\, dz \qquad (40)$$

Where, r_1', and r_2' are the inner and outer radii of the receiver coil. L_1' and L_2' are the lower and upper height of the receiver coil. N' is the turns of receiver coil.
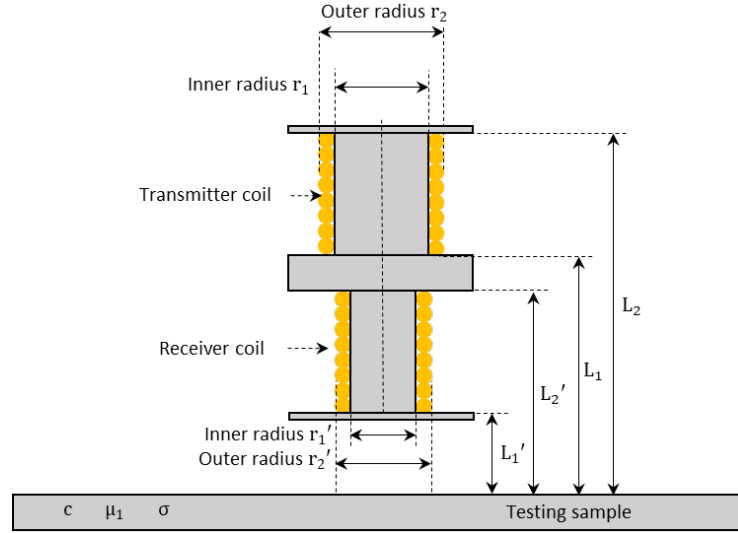
Figure 30 Geometry of air-core inductive sensor (the position of transmitter and receiver is not restricted as the plot; this plot only depicts and denotes the parameters of transmitter-receiver-sample system)

As shown in Fig. 30, further deductions from equation (40), the changes of the impedance (with the presence of sample and in the free space) is

$$Z = \frac{j\pi\mu_0\omega NN'}{(L_2 - L_1)(r_2 - r_1)(L_2' - L_1')(r_2' - r_1')} \int_0^\infty \frac{P(\alpha)P'(\alpha)}{\alpha^6} H(\alpha)\phi(\alpha)\, d\alpha \qquad (41)$$

$$H(\alpha) = e^{-\alpha(L_2 + L_2')} - e^{-\alpha(L_1 + L_2')} - e^{-\alpha(L_2 + L_1')} + e^{-\alpha(L_1 + L_1')} \qquad (42)$$

$$P'(\alpha) = \int_{\alpha r_1'}^{\alpha r_2'} \tau J_1(\tau)\, d\tau \qquad (43)$$

This section presented the numerical FEM and analytical Dodd-Deeds formulas for the simulation of EM field and sensor signal (voltage, inductance, or impedance). The analytical Dodd-Deeds formulas is suitable for test piece with symmetric geometry and properties, which the numerical FEM applies to the samples with irregular (asymmetric) geometry and even anisotropic properties.

Chapter 7 Conclusion and Future Work

The published works related to one of the most promising sensing devices - the electromagnetic (EM) sensor, which is utilised to test both ferromagnetic and non-ferromagnetic samples. To retrieve the properties of metallic structure, several sensor designs and features using the modified Dodd-Deeds method have been found for diverse applications, such as the retrieval of electrical conductivity or magnetic permeability of ferromagnetic samples (Chapter 3), thickness measurement of non-magnetic samples (Chapter 4), evaluation of thickness for coatings above ferromagnetic steel (Chapter 5), and determination of surface crack orientation on ferromagnetic steel (Chapter 5). To simulate the EM field, an acceleration method has been developed to hasten the canonical edge-element FEM, particularly for the modelling computation of probes scanning over surface defects of metals (Chapter 6).

The contributed papers have been published in the top journals in electricity and electronic engineering field, which reflects peers' recognition of the value of this research.

The aim of this work is improving non-destructive testing of metals or steels based on electromagnetic computation methods. Robust systems for the electromagnetic properties measurement of a sample or component are significantly desirable for the reconstruction and detection of the object, particularly for the quality inspection of the sample in the industrial production process. The electromagnetic measurement systems described in this work retrieved multiple properties (conductivity, permeability, thickness, and lift-off - i.e., the distance between the eddy current sensor and test piece). Moreover, non-contact measurement of the eddy current testing provided a safe and precise measurement environment without impairing the samples (especially for the high elastic, high extension, and contact sensitive material samples). Most importantly, the electromagnetic measurement system developed in this work compensated the measurement error caused by the lift-off (separation distance) between the sensor and sample. The developed electromagnetic measurement systems can be applied in diverse fields such as the industrial quality inspector, safety checker, petroleum detection, and food security.

7.1 EM eddy-current sensor and monitoring system for property measurement of ferromagnetic slabs

7.1.1 Permeability invariance phenomenon (measurement of electrical conductivity)

a. Conclusion of published work

A permeability invariance phenomenon with an optimised lift-off was found when using a drive-pickup eddy current sensor. It was discovered that at certain lift-off, the influence of magnetic permeability on measured inductance is eliminated. This phenomenon is used to retrieve the electrical conductivity of ferrous plates when the permeability is unknown. The optimised lift-off is sensor dependent and strongly relates to the spacing between the transmitter and the receiver (drive-pickup sensor). In addition, the effects of permeability range, excitation frequency and sample thickness on the permeability invariance lift-off were all analysed (the valid ranges were provided for the sensor with specific dimensions, which varies with different sensor setups).

b. Future work

The permeability invariance feature is merely based on the drive-pickup eddy-current sensor. Besides, the optimal lift-off varies with the spacing between the drive transmitter and pickup receiver. Moreover, the developed method cannot apply to the lift-off variations when the sensor vibrates. Further investigations will be undertaken on seeking the relationship between the optimal lift-off and transmitter-receiver spacing, and the strategies on compensating the error due to lift-off variations, which will provide an optimal sensor setup (pole spacing between the transmitter and receiver) for the measurement system that requires different ranges of lift-offs (on retrieving the conductivity with unknow magnetic permeabilities).

7.1.2 Single-frequency phase feature (measurement of permeability)

a. Conclusion of published work

A planar triple-coil EM sensor was designed, which is composed of one transmitter and two receivers with different radii (co-axially assembled in the same lift-off plane). By combining the measured impedance from the dual transmitter-receiver sensing pairs at a single-frequency, a simplified (impedance) phase algorithm (based on the Dodd-Deeds analytical formulas) was developed for the permeability measurement of ferromagnetic specimens while reducing the lift-off effects.

b. Future work

Although the single-frequency phase feature of the planar triple-coil sensor does not need to concern the magnitude discrepancy between the model and measurement, the impedance phase is less sensitive to the test piece particularly at low frequencies (lower than around 1 kHz) or high working frequencies (frequencies higher than around 100 kHz). Thus, considering the sensitivities of measured signals to the metal parameters, alternating features that apply to an extensive range of frequencies are required in the future.

7.1.3 Dual-frequency linearity and lift-off insensitive inductance features (measurement of lift-offs and EM properties)

a. Conclusion of published work

Two high-frequency features were found from the triple-coil sensor. Firstly, a dual-frequency linearity feature was found, where the lift-off of sensor (a custom-built concentric triple-coil eddy current sensor) was found to be linear with the ratio of dual-frequency (high frequency) inductance change from dual sensing pairs. Secondly, a lift-off insensitive inductance feature (independent of the test sample and less affected by the lift-off) was found to further mitigate the influence of lift-offs. The EM properties of ferromagnetic steels were retrieved from the corresponding frequency of the lift-off insensitive inductance. Based on these two features, simplified algorithms (from Dodd-Deeds analytical formulas) have been developed to directly retrieve the lift-off and EM properties of ferromagnetic steels.

b. Future work

Simplified algorithms based on the high-frequency features (dual-frequency linearity and lift-off insensitive features) only apply to the concentric triple-coil sensor. The sensor is more complex than the single transmitter-receiver sensing pair and need to mitigate the error due to the magnetic imbalance (from two sensing coils). In the future, simplifications and features on the property retrieval will be focused on the single transmitter-receiver sensing pair.

Besides, algorithms embedded in the retrieval system are based on the air-core coil setup. The air-core sensor is intended to be deployed in the furnace for the high-temperature environment measurement (where the steel slice of ferrite cores will melt). For the room temperature environment, ferrite-core sensors may be required for the hysteresis analysis of ferromagnetic steels with high relative permeabilities (over 1000, e.g., electrical steels, where a strong magnetic H field is required for the magnetization). Future research will be extended to analyse the hysteresis of steels (using ferrite-core sensor) while compensating the lift-off effects. Moreover, apart from the planar slabs, more analyses will be conducted on the property retrieval of samples with other geometries (e.g., pipes, slabs with spherical surface).

7.2 EM eddy-current sensor for thickness measurement of non-magnetic plates

7.2.1 Single-frequency phase feature (based on the planar triple-coil sensor design)

a. Conclusion of published work

Based on a planar triple-coil sensor, a single-frequency algorithm was developed to retrieve the thickness of the non-magnetic metallic plate from the measured inductance phase of two transmitter-receiver coils pair with different radii (on the same lift-off plane). Compared to the thickness retrieval methods using the swept-frequency (or multi-frequency) measurement strategies, only a single-frequency measurement is

required, which avoids complicated instrument setups (e.g., multi-frequency channel instrument or sensor arrays for the multi-frequency testing).

b. Future work

Since the impedance phase is less sensitive to the test piece particularly at low frequencies (lower than around 1 kHz) or high working frequencies (frequencies higher than around 100 kHz), the measurement strategy using the single-frequency phase feature of the planar triple-coil sensor needs to be improved. Considering the sensitivity of measured signals to the thickness, more features and measurement strategies will be investigated to increase the sensitivity of sensor signals (to parameters of test pieces) in the future.

7.2.2 High frequency-regime – quiescent inductance feature of simplified Dodd-Deeds algorithm (based on the single-sensing pair)

a. Conclusion of published work

A quiescent inductance feature was found using a single transmitter-receiver (coaxially wound) sensing pair. That is, the inductance was found sensitive to the lift-off distance and independent of the test piece at an optimal single high working frequency (over 1 kHz). Simplified algorithms were developed based on the quiescent inductance feature for the retrieval of both lift-offs and thickness of non-magnetic laminates. Compared to the triple-coil sensor setup, the single sensing pair is less mechanically complicated and avoids the error that may be caused by the misbalance of magnetic field (triple-coil setup).

b. Future work

The developed algorithm for inversion of lift-offs and thicknesses only applies to the single-layer non-ferromagnetic plate. An additional layer, or even a permeable ferromagnetic layer can affect the magnitude and phase of measured signals. Therefore, it is recommended to explore a multi-layer version of the developed method (e.g., the thickness measurement of non-ferromagnetic coatings on ferromagnetic substrates).

The developed methods apply to the thickness evaluation of planar steels in the production process – using air-core sensors interrogating metallic plates (under high temperature environment). Future research will be emphasised on the thickness or defect evaluation of pipes or other curved metallic plates. Besides, ferrite cores may be required to augment signals and increase the sensitivities of sensors. Thus, it is recommended to explore methods for evaluating thickness of non-ferromagnetic laminates using the ferrite-core eddy current sensor.

7.2.3 High-frequency linearity feature (based on the planar triple-coil sensor design) and pancake sensor

a. Conclusion of published work

A high-frequency linearity feature was found using the planar triple-coil (with different radii) sensor. That is, the ratio between the real part and imaginary part of the integrand (in the Dodd-Deeds formulas) is linear at high frequencies (generally for frequencies over 1 kHz). Based on this high-frequency linearity feature, simplifications have been made on the Dodd-Deeds formulas for the retrieval of both lift-offs and thickness of non-magnetic plates. Besides, a lift-off tolerant pancake sensor was designed for the signal augmentation (as the coil signal significantly attenuates with lift-offs) and extension of the range capability on retrieving lift-offs. By analysing the sensitive region of the magnetic vector potential change (due to the test piece), the receiver of the sensor was designed as a circular spiral pancake coil with a large mean radius and span length (the difference between inner and outer radius). Compared to other techniques on lift-off compensation (e.g., peak frequency feature of multi-frequency inductance), the developed algorithms with pancake sensor (for the signal augmentation) directly retrieved the thickness and lift-offs of up to 15 mm (the maximum lift-off for the previous peak frequency feature was around 5 mm).

b. Future work

Both the high-frequency linearity feature and pancake sensing strategy are based on the measurement of triple coils (or the dual transmitter-receiver sensing pairs), which are more complex than the single transmitter-receiver sensing pair and need to mitigate the error due to the magnetic imbalance (from two

sensing coils). Thus, the features and pancake sensor need to be blended in the single transmitter-receiver sensing pair.

7.2.4 Single-frequency algorithms for the thickness retrieval of circular laminates in real-time while reducing the lift-off effect (based on the triple-coil sensor design)

a. Conclusion of published work

Previously, methods of thickness retrieval only applied to the metallic plate with large planar size (at least 5 times of the coil diameter), as the planar size of test piece was treated as infinite in the analytical Dodd-Deeds model. In my published work, simplification and revision were made on the original Dodd-Deeds formulas to calculate the inductance for coils above a finite-size circular metallic plate when using the custom-built concentric triple-coil eddy current sensor. Algorithms were developed for the first time to retrieve the thickness of finite-size circular metallic plates while compensating the lift-off errors. The retrieval was based on the single-frequency inductance (change due to the test piece) of the concentric triple-coil eddy current probe, which is suitable for the real-time measurement of thickness and do not need recalibrations.

b. Future work

The developed retrieval technique only applies to the situation when the coil is concentric to the circular metallic plates. Theoretically, an offset between the axial of coils and circular plates could result in a reduced inductance change (due to the test piece), which could lead to an underestimated thickness. In the future, more investigations will be conducted on compensating the retrieval error caused by the offset between the axial of coils and circular plates.

7.3 Other retrieval applications – thickness measurement of coatings, and determination of surface-defect orientation on ferromagnetic steels

7.3.1 Evaluation of coating thickness based on lift-off insensitive inductance feature of triple-coil (concentric) sensor

a. Conclusion of published work

Previous techniques on the thickness retrieval only applies to single-layer non-ferromagnetic metal plates. In my published article, a lift-off insensitive inductance feature was found for the first time for circular coils above coated ferromagnetic steels. That is, for the coils above the dual-layer metallic structure of a non-ferromagnetic metallic coating on the ferromagnetic substrate, swept-frequency inductance curves of different lift-offs intersect at a point. Moreover, the inductance value of the intersected point only depends on the sensor parameters (and immune to the test piece). The frequency of the intersected point, termed as the lift-off insensitive frequency, is used to retrieve the thickness of coatings.

b. Future work

The developed method on thickness retrieval of coatings applies to the dual-layer metallic plate. Besides, the coating and substrate were assumed as non-ferromagnetic and ferromagnetic materials, respectively. In the future, it is recommended to explore more features or a general method (if possible) on the retrieval of coating thickness on applications of different material combinations (e.g., the multiple-layer substrate with both non-ferromagnetic and ferromagnetic layers).

7.3.2 Determination of surface crack orientation based on a revised eddy-current thin-skin regime of triple-coil drive-pickup (with horizontal pole spacing) sensor

a. Conclusion of published work

The original eddy-current thin-skin regime applied to the computation of the voltage for a circular eddy-current coil above an ideal surface crack on planar steel. In my published article, a revised version of eddy-current thin-skin regime was developed for the voltage computation of a custom-built triple-coil drive-pickup scanning over an ideal surface crack with different angles (compared to the scanning direction).

Combining the voltage from two receivers, the orientation of the surface notch was retrieved with an error of 3.5 %. Compared to the previous strategies of determining the crack orientation using a single-coil differential probe, the developed method does not require the physical rotation of the sensor.

b. Future work

In the developed method of determining the surface crack orientation, the variations of depth of the surface crack could slightly affect the retrieved angle. This is because both the crack orientation and depth affect the probe voltage. In the future, it is suggested to combine the developed method with the rotating-field method. That is, using the rotating-field method to determine the depth of crack (which is immune to the crack orientation), then using the developed method for the retrieval of crack orientation.

Besides, since the developed method is based on the eddy-current thin-skin regime, the angle retrieval only applies to the long crack (compared to the sensor diameter). In the future, more methods will be explored to the short (or narrow) crack, and even inclined crack cases.

7.4 3-D EM finite-element modelling software for eddy-current non-destructive testing

a. Conclusion of published work

A novel acceleration strategy based on the FEM was developed to hasten the electromagnetic simulation of process for the probe scanning over surface defects of metals. Based on the BICGS (Bi-conjugate gradients stablished) processing methods, the solution (eddy currents and induced voltages on coils) of the previous probe position step was used as the initial guess (the default value is zero) for the solving of next adjacent one. With the developed acceleration strategy, around 40 % of the computation time is reduced.

b. Future work

The developed method merely exploited the finite-element method for the simulations of eddy current testing. In order to further hasten the computations, it is suggested to blend the developed acceleration strategy into a combined method - the finite-element method with boundary conditions (i.e., combining finite element method with boundary element condition/method) for specific modelling situations (e.g., surface crack scanning and swept-frequency impedance measurement of sensor above plates).

References

AbdAlla, A.N., Faraj, M.A., Samsuri, F., Rifai, D., Ali, K. and Al-Douri, Y., 2019. Challenges in improving the performance of eddy current testing. Measurement and Control, 52(1-2), pp.46-64.

Angani, C.S., Ramos, H.G., Ribeiro, A.L., Rocha, T.J. and Baskaran, P., 2016. Lift-off point of intersection feature in transient eddy-current oscillations method to detect thickness variation in stainless steel. IEEE Transactions on Magnetics, 52(6), pp.1-8.

Auld, B.A. and Moulder, J.C., 1999. Review of advances in quantitative eddy current nondestructive evaluation. Journal of Nondestructive evaluation, 18(1), pp.3-36.

Bíró, O., 1999. Edge element formulations of eddy current problems. Computer methods in applied mechanics and engineering, 169(3-4), pp.391-405.

Blitz, J. and Simpson, G., 1995. Ultrasonic methods of non-destructive testing (Vol. 2). Springer Science & Business Media.

Blitz, J., 2012. Electrical and magnetic methods of non-destructive testing (Vol. 3). Berlin: Springer Science & Business Media.

Bowler, J. and Johnson, M., 1997. Pulsed eddy-current response to a conducting half-space. IEEE Transactions on magnetics, 33(3), pp.2258-2264.

Bowler, N., 2006. Theory of four-point alternating current potential drop measurements on a metal half-space. Journal of Physics D: Applied Physics, 39(3), p.584.

Cartz, L., 1995. Nondestructive testing. Ohio:ASM International.

Chew, W.C., 1995. Waves and fields in inhomogeneous media. New York, NY USA: IEEE press. chapter 2.

Davis, C.L., Papaelias, M.P., Strangwood, M. and Peyton, A., 2002. Measurement of phase transformation in steels using electromagnetic sensors. Ironmaking & steelmaking, 29(6), pp.469-476.

Dickinson, S.J., Binns, R., Yin, W., Davis, C. and Peyton, A.J., 2007. The development of a multifrequency electromagnetic instrument for monitoring the phase transformation of hot strip steel. IEEE Transactions on Instrumentation and Measurement, 56(3), pp.879-886.

Dodd, C.V. and Deeds, W.E., 1968. Analytical solutions to eddy-current probe-coil problems. Journal of applied physics, 39(6), pp.2829-2838.

Dwivedi, S.K., Vishwakarma, M. and Soni, A., 2018. Advances and researches on non destructive testing: A review. Materials Today: Proceedings, 5(2), pp.3690-3698.

Fan, M., Cao, B., Tian, G., Ye, B. and Li, W., 2016. Thickness measurement using liftoff point of intersection in pulsed eddy current responses for elimination of liftoff effect. Sensors and Actuators A: Physical, 251, pp.66-74.

Fritschy, J., Horesh, L., Holder, D.S. and Bayford, R.H., 2005. Using the GRID to improve the computation speed of electrical impedance tomography (EIT) reconstruction algorithms. Physiological measurement, 26(2), p.S209.

García-Martín, J., Gómez-Gil, J. and Vázquez-Sánchez, E., 2011. Non-destructive techniques based on eddy current testing. Sensors, 11(3), pp.2525-2565.

Georgii, J. and Westermann, R., 2010. A streaming approach for sparse matrix products and its application in Galerkin multigrid methods. Electronic Transactions on Numerical Analysis, 37(263-275), pp.3-5.

Giguère, J.S.R., Lepine, B.A. and Dubois, J.M.S., 2002, May. Detection of cracks beneath rivet heads via pulsed eddy current technique. In AIP Conference Proceedings (Vol. 615, No. 1, pp. 1968-1975). American Institute of Physics.

Gödel, N., Schomann, S., Warburton, T. and Clemens, M., 2010. GPU accelerated Adams–Bashforth multirate discontinuous Galerkin FEM simulation of high-frequency electromagnetic fields. IEEE Transactions on magnetics, 46(8), pp.2735-2738.

Harfield, N. and Bowler, J.R., 1997. Theory of thin-skin eddy-current interaction with surface cracks. Journal of applied physics, 82(9), pp.4590-4603.

Harrison, D.J., 1994. Eddy-current inspection using Hall sensors and transient excitation. Defence Research Agency Technical Report DRA/SMC/TR941008, DRA Farnborough, UK.

Huang, R., Lu, M., Peyton, A. and Yin, W., 2020. Thickness measurement of metallic plates with finite planar dimension using eddy current method. IEEE Transactions on Instrumentation and Measurement, 69(10), pp.8424-8431.

Huang, R., Lu, M., Zhang, Z., Zhao, Q., Xie, Y., Tao, Y., Meng, T., Peyton, A., Theodoulidis, T. and Yin, W., 2020. Measurement of the radius of metallic plates based on a novel finite region eigenfunction expansion (FREE) method. IEEE Sensors Journal, 20(24), pp.15099-15106.

Hull, J.B. and John, V., 2015. Non-destructive testing. New York: Macmillan International Higher Education.

Jella, P.K., 2004. Automated compensation and classification algorithms for array probe eddy current nondestructive evaluation. Michigan State University, p.32.

Johnson, H.H., 1965. Calibrating the electric potential method for studying slow crack growth. Mater Res Stand 5, pp.442–445.

Kim, D., Udpa, L. and Udpa, S., 2004. Remote field eddy current testing for detection of stress corrosion cracks in gas transmission pipelines. Materials Letters, 58(15), pp.2102-2104.

Knight, M.J., Brennan, F.P. and Dover, W.D., 2004. Effect of residual stress on ACFM crack measurements in drill collar threaded connections. NDT & E International, 37(5), pp.337-343.

Lenzi, M.S., Lefteriu, S., Beriot, H. and Desmet, W., 2013. A fast frequency sweep approach using Padé approximations for solving Helmholtz finite element models. Journal of Sound and Vibration, 332(8), pp.1897-1917.

Li, Y., Theodoulidis, T. and Tian, G.Y., 2007. Magnetic field-based eddy-current modeling for multilayered specimens. IEEE Transactions on magnetics, 43(11), pp.4010-4015.

Liu, S., Sun, Y., Gu, M., Liu, C., He, L. and Kang, Y., 2017. Review and analysis of three representative electromagnetic NDT methods. Insight-Non-Destructive Testing and Condition Monitoring, 59(4), pp.176-183.

Liu, Y. and Yuan, J., 2006. A finite element domain decomposition combined with algebraic multigrid method for large-scale electromagnetic field computation. IEEE transactions on magnetics, 42(4), pp.655-658.

Liu, Z., Tsukada, K., Hanasaki, K. and Kurisu, M., 1999. Two-dimensional eddy current signal enhancement via multifrequency data fusion. Journal of Research in Nondestructive Evaluation, 11(3), pp.165-177.

Lu, M., Chen, L., Meng, X., Huang, R., Peyton, A. and Yin, W., 2021. Thickness measurement of metallic film based on a high-frequency feature of triple-coil electromagnetic eddy current sensor. IEEE Transactions on Instrumentation and Measurement, 70, pp.1-8.

Lu, M., Meng, X., Chen, L., Huang, R., Yin, W. and Peyton, A., 2020. Measurement of ferromagnetic slabs permeability based on a novel planar triple-coil sensor. IEEE Sensors Journal, 20(6), pp.2904-2910.

Lu, M., Meng, X., Huang, R., Chen, L., Peyton, A. and Yin, W., 2021. Measuring lift-off distance and electromagnetic property of metal using dual-frequency linearity feature. IEEE Transactions on Instrumentation and Measurement, 70, pp.1-9.

Lu, M., Meng, X., Huang, R., Chen, L., Peyton, A. and Yin, W., 2021. Lift-off Tolerant Pancake Eddy-Current Sensor for the Thickness and Spacing Measurement of Nonmagnetic Plates. IEEE Transactions on Instrumentation and Measurement, 70, pp.1-9.

Lu, M., Meng, X., Huang, R., Chen, L., Peyton, A. and Yin, W., 2021. Inversion of Distance and Magnetic Permeability Based on Material-Independent and Lift-off Insensitive Algorithms Using Eddy Current Sensor. IEEE Transactions on Instrumentation and Measurement, 70, pp.1-9.

Lu, M., Meng, X., Huang, R., Chen, L., Peyton, A., Yin, W. and Qu, Z., 2021. Thickness measurement of circular metallic film using single-frequency eddy current sensor. NDT & E International, p.102420.

Lu, M., Meng, X., Huang, R., Chen, L., Tang, Z., Li, J., Peyton, A. and Yin, W., 2021. Determination of Surface Crack Orientation Based on Thin-Skin Regime Using Triple-Coil Drive–Pickup Eddy-Current Sensor. IEEE Transactions on Instrumentation and Measurement, 70, pp.1-9.

Lu, M., Meng, X., Yin, W., Qu, Z., Wu, F., Tang, J., Xu, H., Huang, R., Chen, Z., Zhao, Q. and Zhang, Z., 2019. Thickness measurement of non-magnetic steel plates using a novel planar triple-coil sensor. NDT & E International, 107, p.102148.

Lu, M., Peyton, A. and Yin, W., 2017. Acceleration of frequency sweeping in eddy-current computation. IEEE Transactions on Magnetics, 53(7), pp.1-8.

Lu, M., Yin, L., Peyton, A.J. and Yin, W., 2016. A novel compensation algorithm for thickness measurement immune to lift-off variations using eddy current method. IEEE Transactions on Instrumentation and Measurement, 65(12), pp.2773-2779.

Lu, M., Zhao, Q., Hu, P., Yin, W. and Peyton, A.J., 2015, April. Prediction of the asymptotical magnetic polarization tensors for cylindrical samples using the boundary element method. In 2015 IEEE Sensors Applications Symposium (SAS) (pp. 1-4). IEEE.

Lu, M., Zhu, W., Yin, L., Peyton, A.J., Yin, W. and Qu, Z., 2017. Reducing the lift-off effect on permeability measurement for magnetic plates from multifrequency induction data. IEEE Transactions on Instrumentation and Measurement, 67(1), pp.167-174.

Lu, M., Yin, W.*, Peyton, A.J., Qu, Z., Meng, X., Xie, Y., Zhao, P., Luo, J., Zhao, Q., Tao, Y., Zhou, T., Zhang, Z., 2019. A model for the triboelectric nanogenerator with inductive load and its energy boost potential. Nano energy, 54, pp. 103883.

Ma, J. and Nie, Z.P., 2013. FEM-DDM with an efficient second-order transmission condition in both high-frequency and low-frequency applications. Progress In Electromagnetics Research, 50, pp.253-271.

Mandache, C. and Lefebvre, J.H.V., 2006. Transient and harmonic eddy currents: Lift-off point of intersection. NDT & E International, 39(1), pp.57-60.

Margetts, L., Smith, I.M. and Leng, J.M., 2006, June. Parallel 3D finite element analysis of coupled problems. In III European Conference on Computational Mechanics Solids Structures and Coupled Problems in Engineering, ECCM (pp. 5-8).

Meng, X., Lu, M., Yin, W., Bennecer, A. and Kirk, K.J., 2021. Evaluation of coating thickness using lift-off insensitivity of eddy current sensor. Sensors, 21(2), p.419.

Meng, X., Lu, M., Yin, W., Bennecer, A. and Kirk, K.J., 2021. Inversion of lift-off distance and thickness for non-magnetic metal using eddy current testing. IEEE Transactions on Instrumentation and Measurement, 70, pp.1-8.

Mortarelli, J.R., 1980. A generalization of the Geselowitz relationship useful in impedance plethysmographic field calculations. IEEE Transactions on Biomedical Engineering, (11), pp.665-667.

Nicholson, G.L. and Davis, C.L., 2012. Modelling of the response of an ACFM sensor to rail and rail wheel RCF cracks. NDT & E International, 46, pp.107-114.

Papaelias, M.P., Lugg, M.C., Roberts, C. and Davis, C.L., 2009. High-speed inspection of rails using ACFM techniques. NDT & e International, 42(4), pp.328-335.

Placko, D. and Dufour, I., 1992, October. Eddy current sensors for nondestructive inspection of graphite composite materials. In Conference Record of the 1992 IEEE Industry Applications Society Annual Meeting (pp. 1676-1682). IEEE.

Pohl, R., Erhard, A., Montag, H.J., Thomas, H.M. and Wüstenberg, H., 2004. NDT techniques for railroad wheel and gauge corner inspection. NDT & E International, 37(2), pp.89-94.

Preda, G., Cranganu-Cretu, B., Hantila, F.I., Mihalache, O., Chen, Z. and Miya, K., 2002. Nonlinear FEM-BEM formulation and model-free inversion procedure for reconstruction of cracks using pulse eddy currents. IEEE transactions on magnetics, 38(2), pp.1241-1244.

Raja, M.K., Mahadevan, S., Rao, B.P.C., Behera, S.P., Jayakumar, T. and Raj, B., 2010. Influence of crack length on crack depth measurement by an alternating current potential drop technique. Measurement Science and Technology, 21(10), p.105702.

Rodriguez, S., Xie, Y., Yin, W. and Peyton, A.J., 2014, October. A FPGA Based Platform for Multi-Frequency Eddy Current Testing. In Proceedings of the 11th European Conference on Non-Destructive Testing (ECNDT 2014) (pp. 6-10).

Schrefl, T., Fidler, J., Kirk, K.J. and Chapman, J.N., 1997. A higher order FEM-BEM method for the calculation of domain processes in magnetic nano-elements. IEEE Transactions on Magnetics, 33(5), pp.4182-4184.

Sekine, K., Kasai, N. and Maruyama, H., 2000. The non-destructive evaluation method for far-side corrosive type flaws in steel plates using magnetic flux leakage technique. In 15th World Conference on Non-Destructive Testing (WCNDT).

Sfarra, S., Ibarra-Castanedo, C., Ambrosini, D., Paoletti, D., Bendada, A. and Maldague, X., 2014. Discovering the defects in paintings using non-destructive testing (NDT) techniques and passing through measurements of deformation. Journal of Nondestructive Evaluation, 33(3), pp.358-383.

Theodoulidis, T., 2005. Analytical model for tilted coils in eddy-current nondestructive inspection. IEEE transactions on magnetics, 41(9), pp.2447-2454.

Theodoulidis, T., 2010. Developments in efficiently modelling eddy current testing of narrow cracks. NDT & E International, 43(7), pp.591-598.

Theodoulidis, T.P. and Bowler, J.R., 2005, April. The truncated region eigenfunction expansion method for the solution of boundary value problems in eddy current nondestructive evaluation. In AIP Conference Proceedings (Vol. 760, No. 1, pp. 403-408). American Institute of Physics.

Thomas, H.M., Dey, A. and Heyder, R., 2010. Eddy current test method for early detection of rolling contact fatigue (RCF) in rails. Insight-Northampton, 52(7), p.361.

Tian, G.Y. and Sophian, A., 2005. Reduction of lift-off effects for pulsed eddy current NDT. NDT & E International, 38(4), pp.319-324.

Udpa, S. S. and Stanley, R. K., 2004. Magnetic flux leakage testing. In Udpa S. S. and Moore P. O., editors, Electromagnetic Testing, volume 5 of Nondestructive Testing Handbook, pages 227-245. American Society of Nondestructive Testing, Columbus, OH, 3rd edition.

Vassilaros, M.G. and Hackett, E.M., 1984, January. J-integral R-curve testing of high strength steels utilizing the direct-current potential drop method. In Fracture Mechanics: Fifteenth Symposium. ASTM International.

Wang, Y., Fan, M., Cao, B., Ye, B. and Wen, D., 2020. Measurement of coating thickness using lift-off point of intersection features from pulsed eddy current signals. NDT & E International, 116, p.102333.

Wen, D., Fan, M., Cao, B., Ye, B. and Tian, G., 2018. Extraction of LOI features from spectral pulsed eddy current signals for evaluation of ferromagnetic samples. IEEE Sensors Journal, 19(1), pp.189-195.

Xin, J., Lei, N., Udpa, L. and Udpa, S.S., 2013. Rotating field eddy current probe with bobbin pickup coil for steam generator tubes inspection. NDT & E International, 54, pp.45-55.

Xu, X., Liu, M., Zhang, Z. and Jia, Y., 2014. A novel high sensitivity sensor for remote field eddy current non-destructive testing based on orthogonal magnetic field. Sensors, 14(12), pp.24098-24115.

Yin, W. and Peyton, A.J., 2007. Thickness measurement of non-magnetic plates using multi-frequency eddy current sensors. NDT & E International, 40(1), pp.43-48.

Yin, W., Hao, X.J., Peyton, A.J., Strangwood, M. and Davis, C.L., 2009. Measurement of permeability and ferrite/austenite phase fraction using a multi-frequency electromagnetic sensor. NDT & E International, 42(1), pp.64-68.

Yin, W., Lu, M., Tang, J., Zhao, Q., Zhang, Z., Li, K., Han, Y. and Peyton, A., 2018. Custom edge-element FEM solver and its application to eddy-current simulation of realistic 2M-element human brain phantom. Bioelectromagnetics, 39(8), pp.604-616.

Yin, W., Lu, M., Yin, L., Zhao, Q., Meng, X., Zhang, Z. and Peyton, A., 2018. Acceleration of eddy current computation for scanning probes. Insight-Non-Destructive Testing and Condition Monitoring, 60(10), pp.547-555.

Yin, W., Meng, X., Lu, M., Zhao, Q., Xu, H., Zhang, Z. and Peyton, A., 2019. Permeability invariance phenomenon and measurement of electrical conductivity for ferrite metallic plates. Insight-Non-Destructive Testing and Condition Monitoring, 61(8), pp.472-479.

Zeng, Z., Udpa, L., Udpa, S.S. and Chan, M.S.C., 2009. Reduced magnetic vector potential formulation in the finite element analysis of eddy current nondestructive testing. IEEE transactions on magnetics, 45(3), pp.964-967.

Zhao, K., Vouvakis, M.N. and Lee, J.F., 2006. Solving electromagnetic problems using a novel symmetric FEM-BEM approach. IEEE Transactions on magnetics, 42(4), pp.583-586.

Zhou, W., Lu, M., Chen, Z., Zhou, L., Yin, L., Zhao, Q., Peyton, A., Li, Y. and Yin, W., 2018. Three-dimensional electromagnetic mixing models for dual-phase steel microstructures. Applied Sciences, 8(4), p.529.